electronics

Article

Performance Evaluation of a Low-Cost Semitransparent 3D-Printed Mesh Patch Antenna for Urban Communication Applications

Luis Inclán-Sánchez

Department of Signal Theory and Communications, Universidad Carlos III de Madrid, 28911 Leganés, Spain; linclan@ing.uc3m.es

Abstract: This study explores the possibility of designing simple semitransparent antennas that allow for the passage of most visible light while maintaining good electromagnetic performance. We propose a substrateless metal mesh patch antenna manufactured using low-cost 3D printing and silver conductive paint. Our goal is to integrate numerous such radiators onto office building windows, preserving natural lighting with minimal visual impact, aiming to alleviate infrastructure congestion or improve antenna placement in sub-6 GHz frequency bands. In this paper, we conduct an analysis of the primary parameters influencing patches constructed with substrateless metal mesh wires, focusing on the grid topology and the width of the metallic wires, as well as their effects on antenna transparency and back radiation. Owing to the absence of a substrate, the antenna demonstrates minimal losses. Furthermore, in this study, we thoroughly investigate the effects of conductivity and roughness on surfaces printed with metallic paint. A prototype at 2.6 GHz is presented, achieving over 60% transparency, a 2.7% impedance-matching bandwidth, and a realized peak gain of 5.4 dBi. The antenna is easy to manufacture and cost-effective and considers sustainability. Its large-scale implementation can alleviate building infrastructure, enhancing radio connectivity in urban environments and offering new cost-effective and energy-efficient wireless solutions.

Keywords: optically transparent antenna; patch antenna; metal mesh; metal grid; 3D printing; substrateless antenna; low-cost antenna; surface roughness; effective conductivity; sustainable materials

check for updates

Citation: Inclán-Sánchez, L. Performance Evaluation of a Low-Cost Semitransparent 3D-Printed Mesh Patch Antenna for Urban Communication Applications. *Electronics* **2024**, *13*, 153. https://doi.org/10.3390/electronics13010153

Academic Editors: Raad Raad, Ladislau Matekovits and Faisel Tubbal

Received: 7 December 2023
Revised: 25 December 2023
Accepted: 27 December 2023
Published: 29 December 2023

1. Introduction

We are witnessing rapid advancements in radio systems, primarily driven by the widespread implementation of 5G technology and strategic planning for the imminent era of 6G [1]. The increasing availability of frequency bands and the coexistence of diverse applications, including communications, sensors, vehicle guidance, and the Internet of Things (IoT), emphasize the growing need for versatile high-efficiency devices.

Within this landscape of multifaceted systems, each demanding exceptional capabilities in terms of latency, ubiquity, and low power consumption [1], it has become imperative to explore innovative approaches to radio device design. Prioritizing elements such as sustainable network development [2], energy efficiency, and minimization of visual or radioelectric impact is crucial. Ultimately, these systems must demonstrate economic viability and energy efficiency while reducing their environmental footprint during manufacturing and maximizing recyclability.

Another challenge arises from the vast number of devices that will need to coexist, motivating an increased need for adequate physical space to accommodate radio systems [1,3]. These locations must facilitate new applications while providing enough space for the multiple antennas and arrays necessary for configurations like massive MIMO. Additionally, they must adhere to rigorous security standards across all radio applications [1]. This approach relates to the concept of Smart Cities [4], integrating infrastructure and network capacity into urban planning from its inception [4] or improving connectivity [5] and ultimately addressing the capacity and coexistence challenges of future 5G/6G wireless systems. In these Smart Cities, reconciling old and new networks is imperative, often requiring buildings and infrastructure to have additional access points, smart surfaces, antennas, and signal repeaters. An emerging possibility is the use of windows and architectural glass surfaces in buildings and vehicles as antenna locations to ensure enough physical space for radio systems. Seeking to maintain the use of natural light and minimize visual impact, there is substantial interest in designing optically transparent antennas that allow for the passage of most visible light [4,6].

The state of the art in transparent antenna design has utilized two main approaches [6]. The first involves designing the entire antenna using transparent materials. In this scenario, the antenna appears invisible, except for limitations in light transmission due to the materials used and non-transparent parts like connectors. Although it is feasible to create conductorless transparent antennas using only dielectric materials (DRA) [7], materials for transparent antennas typically fall into two categories: the substrate and the metallic parts. For substrates, materials like PET or PMMA plastics, glass, acrylic, and even water in transparent containers have been used [4,6,8–12]. Regarding the conductive sections, they are made from semiconductor films like transparent conductive oxides (TCOs) doped with conductive particles to enhance their electrical properties [13]. Research conducted using compounds such as ITO, AZO, AgHT, and ZnO aims to achieve high transparency with high electrical conductivity [4,6,14,15]. However, despite progress, these materials still experience greater losses and lack the efficiency of metals found in PCB-based electronics [6].

The second approach involves replacing the solid metal parts of the antenna with a metal mesh or grid [6,8,16,17]. The density of the mesh—or the spacing between the metal wires—must maintain electrical continuity (typically with periods between $\lambda/10$ and $\lambda/20$ [14]) yet be significantly larger than the wavelength for good optical transmission. As the ratio of holes to surface area increases, the antenna's transparency improves at the expense of electromagnetic performance [8,14]. Practically, this mesh remains visible, making the antenna truly semitransparent. Nevertheless, it retains utility by harnessing natural light or reducing visual impact. Previous studies have often employed micromeshes with thin metal wires—often micrometric [14] or even smaller [18]. This seems like an intermediate approach in which the layout of the mesh is less perceived by the naked eye but limits optical transmission according to its density. Overall, this mesh-based approach generally produces better-performing antenna designs [4,6]. In the state of the art, there are numerous mesh antennas with greater efficiency than those that use conductive films [6], even with performance close to their respective non-transparent designs, as is the case described below. Within the realm of mesh-type antennas, besides the aforementioned micromeshes, work has been conducted with larger-sized meshes where the grid or antenna design is notably visible. In this line, PCB techniques have been employed for the metallic parts, followed by cutting off the non-metallic part [17,19], including via laser cutting [20].

In any of these approaches, antenna manufacturing always involves the following stages: (1) manufacturing of conductive films, micro metal meshes, or macro grids using ink-jet processes, PVD, or PCB followed by cutting; (2) the production, purchase, and/or cutting of transparent materials used as substrates; (3) layer adherence through gluing or deposition processes on the material. This process resembles conventional printing technology, but the complexity of the stages and their integration increases.

Regarding the most common applications for transparent antennas, the initial use has been in communications, including integrating antennas into solar cell panels [21,22], vehicle windows or windshields [10], and device screens [23]. They have also been used in RFID applications, motion/presence control, and even smart glasses [24]. New application fields have recently emerged, such as in energy harvesting [25] and instruments for biological applications [26]. Furthermore, transparent versions of recent technologies are gradually emerging, as seen in [27] for SIW technology or in [28] for advanced absorbers. Transparent electronics are mentioned as an area of interest in radiocommunications, involving not just antennas but also other elements like filters [4] or their combinations, giving rise to rectennas [25,29] or filtering antennas [30].

Patch antennas are the most used radiators in the design of transparent antennas, including examples of all the abovementioned approaches [8,11,15,17,30,31]. In this work, we develop the idea suggested in [32], proposing the creation of transparent mesh antennas using 3D printing. The metallic mesh is manufactured from conventional plastic filaments that are later metallized. Because the antenna can be made as one piece or in two easily joinable parts that include mechanical fastening posts, it is possible to create the antenna without a substrate. This idea was used in [33] to propose an optically semitransparent PIFA made in a grid and integrated into a low-coupling 2 $\times$ 2 MIMO configuration. Now, we propose the development of a low-cost, semitransparent 3D printed patch metallized with silver conductive paint (SCP). The most relevant aspects of the design, mesh topology, width of the metal wires, and the tradeoff between electrical behavior and transparency are analyzed. As the antenna does not have a substrate, it experiences fewer losses, which is mainly attributed to the effective conductivity and the surface roughness of the metallic grid elements. These aspects are studied throughout the paper, and some prototypes are characterized to demonstrate the possibility of designing a simple, cost-effective, semitransparent antenna with good radiation performance and advantages in terms of reduced material usage. Such antennas might be interesting for setting up transparent radiant systems and arrays for sub-6 GHz bands in 5G/6G applications. They offer the possibility of being integrated into office building windows, utilizing natural light, and minimizing visual impact to address space limitations, alleviate the capacity of new network infrastructure, or enable optimal antenna placement for specific wireless environments.

2. Semitransparent Mesh Patch Antenna

In this section, we first present the specific application intended for the semitransparent antenna, covering broader aspects related to energy efficiency and resource utilization. Subsequently, we provide detailed information about the mesh patch antenna proposed in this study and its key design aspects.

2.1. Urban Communication Applications: Optical Transparency and Efficient Resource Allocation

Figure 1 illustrates a typical scenario involving the integration of transparent antennas into the network infrastructure of a smart building. It exemplifies potential solutions for antenna systems integrated into existing structures, like older buildings with saturated infrastructure. Additionally, it showcases the strategic placement of these antennas, considering factors such as coverage from base stations, 5G point-to-point radio links, and the radio environment influenced by nearby building layouts.

As shown in Figure 1, the building's primary architectural surface is glass, offering a substantial area for deployment of antennas or large antenna arrays. Considering the dimensions of the windows, even at lower frequencies of 5G/6G, the space occupied by antennas would be minimal, likely positioned at the window's top or bottom, resulting in minimal visual impact. Furthermore, considering typical antenna array surface dimensions of 20–30 cm $\times$ 50 cm for frequencies between 2 and 3 GHz, the shielding at optical frequencies would be practically imperceptible, preserving natural lighting. Figure 1 depicts a potential integration of multiple semitransparent antennas constructed with a metal mesh on a large window or glass facade of an office building. The intended application involves the deployment of a significant array of antennas, enabling the passage of most light with minimal visual impact while forming part of the building's radio infrastructure. Larger antennas for windows could correspond to frequencies below 6 GHz (sub-6 GHz bands). Thus, aside from the space they occupy, a desirable structural characteristic would be a lightweight design for proper attachment to architectural glass.

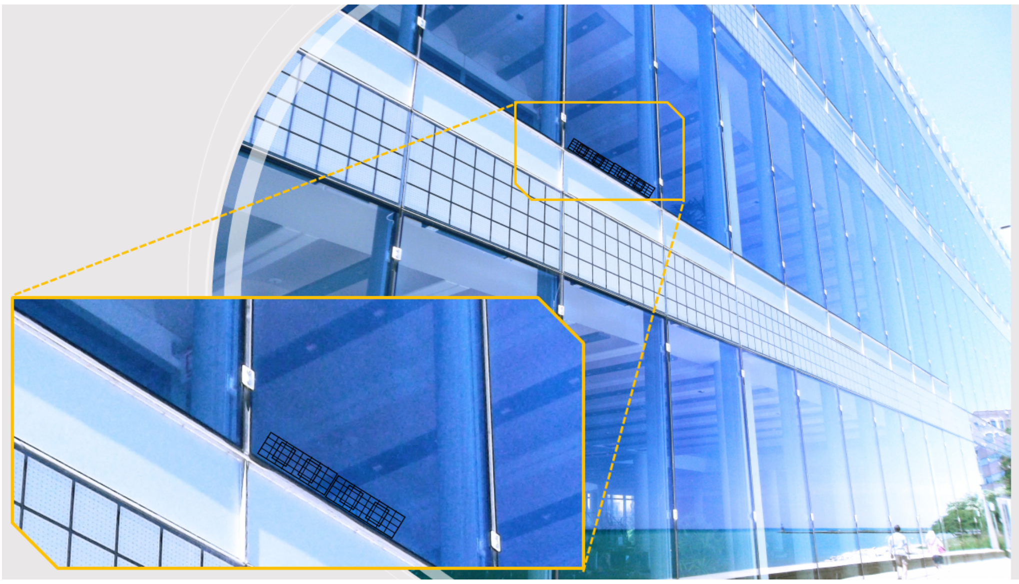

Figure 1. A potential urban application scenario featuring transparent antennas within a smart building. The zoomed-in view illustrates a potential array of semitransparent antennas constructed with metal mesh installed on the window of an office building.

The coexistence of numerous radio systems in urban environments, viewed from the perspective of Smart cities, presents multifunctional challenges with diverse objectives [4,34]. For instance, various wireless network systems coexist within different spatial coverage scales. For example, WiFi has limited coverage, whereas WiMAX and LTE cover broader areas. Different operating frequencies or requirements for power, latency, and data rates present significant variations. Systems like Bluetooth, operating at 2.4 GHz with a range of approximately 1–10 m and a data rate of 1 Mb/s, contrast with more demanding systems like LTE-A, operating at 2.5 GHz or 15 GHz with a coverage of 30 Km and data rates approaching 1 Gb/s in the downlink [34].

In addition to managing coverage and power needs, factors such as spectral efficiency within smart buildings and energy utilization are crucial [34,35]. Energy efficiency is pivotal in terms of network consumption and overall system balance, including buildings' thermal efficiency. Addressing sustainability involves considering waste generation, recycling, and the impact of electronics and network devices [36]. Balancing these aspects necessitates optimization of antennas and technology not only for electromagnetic performance but also for energy utilization, material recycling, manufacturing sustainability, and cost-effectiveness of the process, as depicted in Figure 2. One of the significant advantages of 3D printing lies in its positive impact on sustainability and material recycling. This technique reduces waste by enabling the reuse of surplus material or recycling defective products back into printable material. This ability to utilize and recycle materials, combined with manufacturing precision, aids in reducing the environmental footprint and promoting sustainable practices within the manufacturing industry. In this paper, we specifically utilize cost-effective 3D printing techniques to further explore these sustainability aspects.

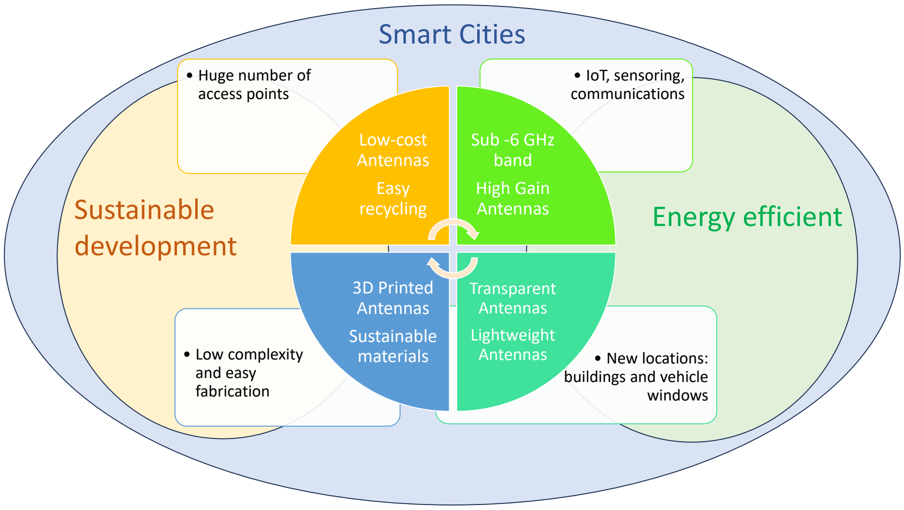

Figure 2. Conceptual scheme of the proposed work. The aim is a low-cost antenna solution operating within the sub-6 GHz band that is suitable for integration into building windows to deploy multiple elements, considering both energy efficiency and resource sustainability.

2.2. Semitransparent Mesh Patch Antenna Description

This section presents the design of a semitransparent antenna made with a metallic mesh. Figure 3 shows the proposed antenna, using the common approach of dividing the metallic surfaces into a grid from a solid metallic patch [4,14,17]. The discretization affects the ground plane and the patch differently, as observed in Figure 3, which also depicts the absence of the substrate and dielectric posts (see Figure 3c) that allow for the mechanical support of the structure. Within this section, we treat the metallic components of the antenna as a lossy conductor. The analysis was conducted using the silver parameters integrated into the CST Studio Suite 2021 simulator. The feeding line is also meshed, in this case using three metallic wires, as shown in Figure 3a, with a width of w = 15.6 mm to provide 50 Ω.

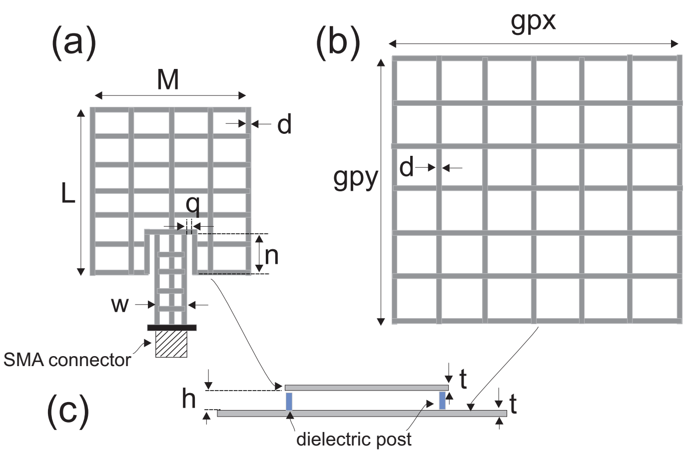

Figure 3. Description of the proposed semitransparent patch antenna and its main geometric parameters: (**a**) patch mesh; (**b**) ground-plane mesh; (**c**) side view with the air layer that replaces the dielectric substrate.

These mesh antennas require a small separation between grid elements compared to the working wavelength. To achieve high electromagnetic field shielding, a separation approximately 10 to 20 times smaller than λ_0 is necessary [14]. In our case, we verified that with larger distances, it is possible to achieve good antenna behavior, although perfect shielding may not be achieved. Our target frequency is 2.6 GHz, and we consider a ground-plane size of $0.56\lambda_0$. This size might seem relatively small, especially considering that a patch antenna typically measures around $\lambda_0/2$ in its fundamental mode. However, we demonstrate that despite its size, it proves adequate to deliver good performance.

We simulated different spacings for the square ground plane of the antenna, as shown in Figure 4, which also includes the main geometric parameters considered for the antenna. As the patch is fed with an inset and considering that the feeding microstrip line is made with three wires, an odd number of elements in the grid is considered in that axis to maintain symmetry, while an even number is chosen in the perpendicular direction. Three transparency levels are compared, corresponding to three different grids: 7 × 8 metal wires (referred to as grid 1), 5 × 6 metal wires (grid 2), and 9 × 10 metal wires (grid 3). With these configurations, we have metallic element distances of $0.19\lambda_0 \times 0.16\lambda_0$ for grid 1, $0.23\lambda_0 \times 0.28\lambda_0$ for grid 2, and $0.14\lambda_0 \times 0.16\lambda_0$ for grid 3. Figure 4 shows the vertical component of the electric field in the antenna's frequency range at 2.5 GHz, 2.6 GHz, and 2.7 GHz for the three grid sizes. The antenna's mode is the fundamental TM_{10}, as shown in Figure 4, with a minimum field in the center and maxima at the ends of the cavity where the patch's fringing fields are excited. It is observed that for all frequencies, as the grid becomes less dense, the electric field penetrates the ground plane to a greater extent. This clearly corresponds to an increasing level of back radiation as the ground-plane metal wires move farther away, as shown in Figure 5. Grid 3 exhibits lower levels of back radiation from the antenna in both planes. Furthermore, in Figure 5, we observe that at all three frequencies, the radiation patterns obtained for grid 1 are very similar to those of grid 3, with a slight increase in the back radiation as the frequency decreases. For the case with the least dense grid (grid 2 of 5 × 6 in Figure 5), the radiation patterns show a substantial increase in back radiation for both planes across the three frequencies.

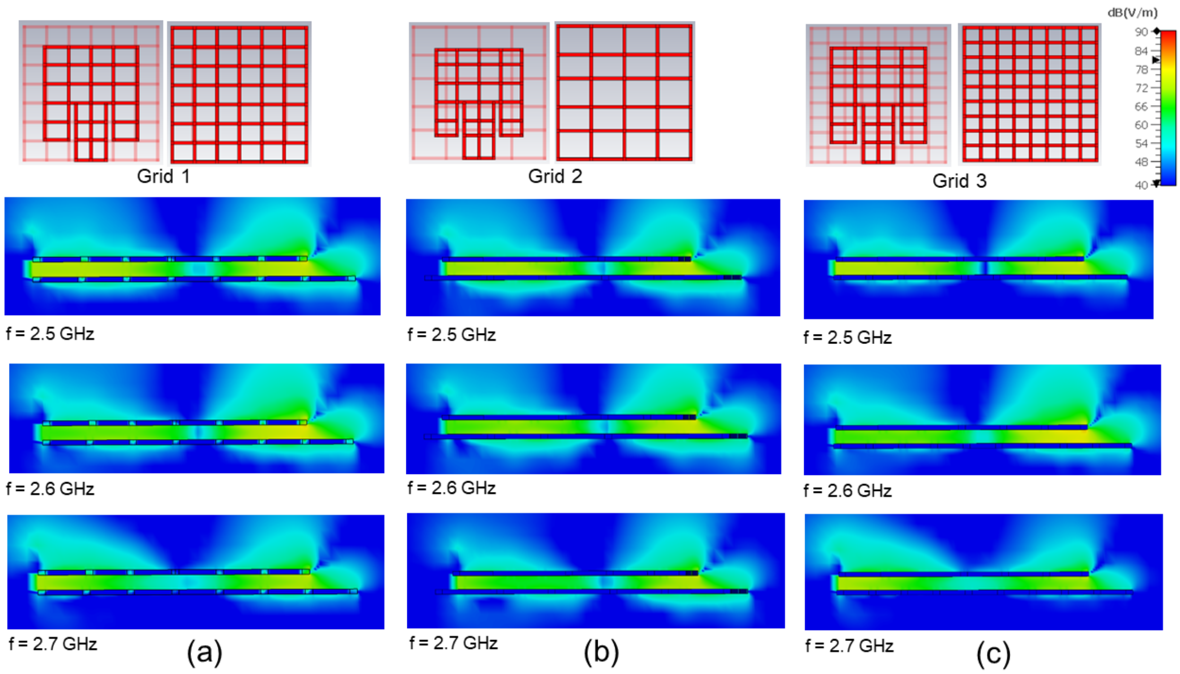

Figure 4. Side view of the |Ez| electric field distribution evaluated for the antenna at different frequencies for the three considered cases of ground-plane metal mesh (gpx = gpy = 64.4 mm, h = 3 mm, t = 1 mm, d = 1.5 mm, q = 1.9 mm): (**a**) 7 × 8 wire mesh (L = M = 45.2 mm and n = 16.3 mm); (**b**) 5 × 6 wire mesh (L = M = 42.4 mm and n = 16.2 mm); (**c**) 9 × 10 wire mesh (L = M = 45.5 mm and n = 16.3 mm).

To choose the mesh topology, one must balance the antenna's electromagnetic behavior with the achievable level of transparency [4,14]. The transparency level, in our case, can be obtained from the following expression [20]:

$$t = 1 - \frac{\sum_{i=1}^{n} A_i}{A_t} \tag{1}$$

where the summation extends over the entire surface occupied by all metallic elements; A_i is the antenna (across both layers if they are not coincident); and A_t is the total area occupied by the antenna, which, in our case, is the total surface of the ground plane. Given that our antenna does not include a substrate, the only elements restricting light transmission in the optical range are its metallic wires (completely opaque in our case). It is clear that the transparency level of the proposed patch depends on the number of wires used for the ground plane and the patch's radiating layer, as well as their lengths and widths.

Given the intended application, the primary merit of the antenna we are considering is its gain. The antenna should exhibit sufficient efficiency for typical applications. It also needs to be planar for seamless integration into buildings. We chose a separation thickness of 3 mm between the ground plane and the patch ($h = 0.026\lambda_0$), making the antenna very flat (approximately 5 mm in total thickness), facilitating its placement on windows. The patch thickness influences its impedance bandwidth, resulting in a narrower bandwidth for the antenna. Transparent mesh-based antennas offer a tradeoff between their degree of transparency on one hand and their gain and resonance frequency on the other [4]. As transparency increases in the patch antenna, its gain decreases, as evidenced by the radiation patterns shown in Figure 5. The resonance frequency can be easily adjusted according to the element's size, but it is important to consider the significant relationship between the transparency and the front-to-back (FTB) ratio of the radiated power of the antenna [33]. There is no doubt that this ratio must be high to improve radio coverage while minimizing interference and exposure levels inside the building. Figure 6 analyzes these effects comprehensively for the three grids considered thus far.

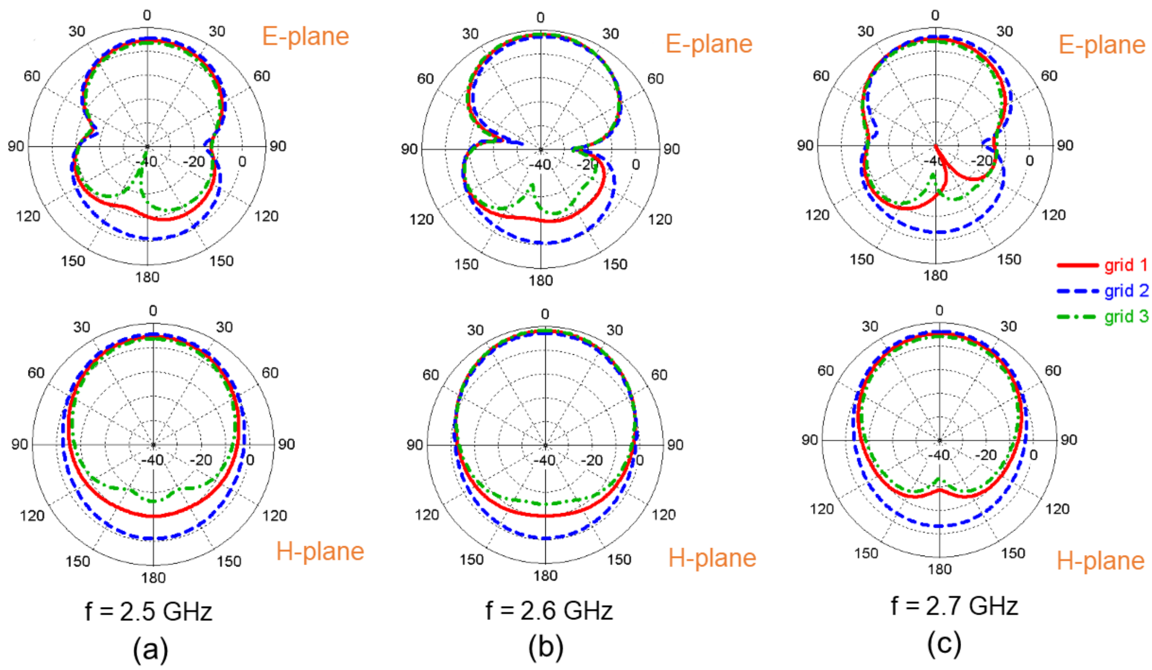

Figure 5. Simulated radiation patterns for the semitransparent antenna for the three ground planes in Figure 7: (grid 1) 7 × 8 wire mesh, (grid 2) 5 × 6 wire mesh, and (grid 3) 9 × 10 wire mesh at different frequencies. (**a**) f = 2.5 GHz; (**b**) f = 2.6 GHz; (**c**) f = 2.7 GHz.

The densest grid (grid 3) yields a gain of 8.3 dB at the working frequency, whereas for the intermediate grid (grid 1), the gain slightly reduces to 8.1 dB. In contrast, the grid with greater separation (grid 2) experiences a decrease in gain down to 7.3 dB at f = 2.6 GHz. It is also noticeable that in this case, although the antenna is matched to the frequency, the highest gain values occur at higher frequencies (2.8–2.9 GHz). The variation in the front-to-back ratio for the antenna relative to the ground plane is much more pronounced. At f = 2.6 GHz, simulation results show FTB values of 24 dB, 18.6 dB, and 8.5 dB for grid 3, grid 1, and grid 2, respectively, as seen in Figure 6. When comparing across grids, clearly, grid 3 and grid 1 offer similar gain values and an FTB increase slightly higher than 5 dB, which is acceptable to enhance transparency. However, when comparing grid 3 with grid 2, a significant decrease in gain is observed, and notably, a substantial increase in back radiation reduces the FTB from 24 dB to 8.5 dB. Clearly, grid 2 does not provide sufficient merit for the application.

In the following sections of this study, we analyze and design a semitransparent patch with an intermediate topology (grid 1), which offers very similar performance to the densely meshed patch but substantially improves its transparency. Applying the expression given by Equation (1), we obtain a transparency of $t = 60.2\%$ for the grid 1 topology with a wire width of d = 1.5 mm.

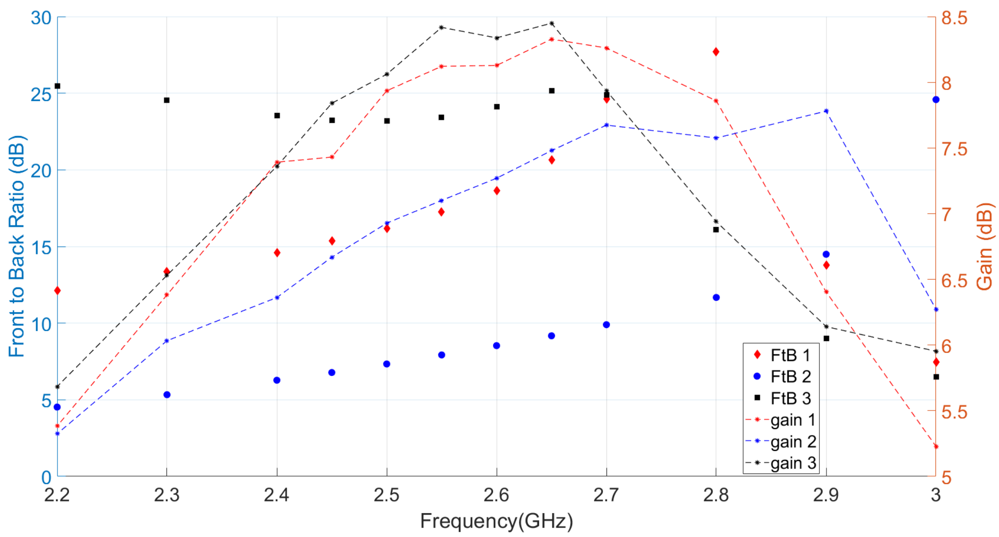

Figure 6. Front to back and gain evaluated for the proposed antenna as a function of frequency for the three ground planes in Figure 7: grid 1 (7 × 8 wires mesh with L = M = 45.2 mm and n = 16.3 mm); grid 2 (5 × 6 wires mesh with L = M = 45.2 mm and n = 16.3 mm); grid 3 (9 × 10 wires mesh with L = M = 45.5 mm and n = 16.3 mm).

Regarding the mesh design for patch metallization, our initial choice involved a 5 × 6 wire configuration. The odd count along the horizontal axis facilitated a wire placement at the center of the feeding point. Additionally, aligning the six wires along the vertical axis, with the lower plane housing the ground plane, helps to enhance the overall transparency, as discussed below. The spacing between elements within the patch mesh did not hinder the proper formation of the antenna cavity, as confirmed in Figure 4. Moving on to Figure 7, the observed $|E_y|$ electric field component aligns with the typical fringing field distribution of the patch. Symmetry and uniformity in the fringing field of the two edges of the resonant side for the patch were maintained for both grid 3 and grid 1, as shown in Figure 7a,b. However, the less dense grid showcased in Figure 7c resulted in a deterioration in both the distribution of the $|E_y|$ component and the current across the wires. Returning to the alignment between antenna layers and utilizing a specific grid similar to grid 1 for the ground plane shown in Figure 8 enables the alignment of wire positions for both the patch's meshed layer and the ground plane's meshed layer, as depicted in Figure 8a,b. This alignment prevents direct visual obstruction through the antenna, enhancing overall transparency, as evidenced in Figure 8c for a manufactured prototype. However, establishing an exact patch size compromises grid uniformity, as evident in the prototype shown in Figure 8c. This slight irregularity, considering wire spacing concerning wavelength, has a minimal impact on the antenna's response. For grid 1, the focal point from this point forward, this effect is minor and was taken into account in the simulations. In the final proposed patch design, besides the obtained gain and FTB values, it was confirmed that the cross-polar components of the radiation patterns remained consistently below −30 dB across all relevant frequencies.

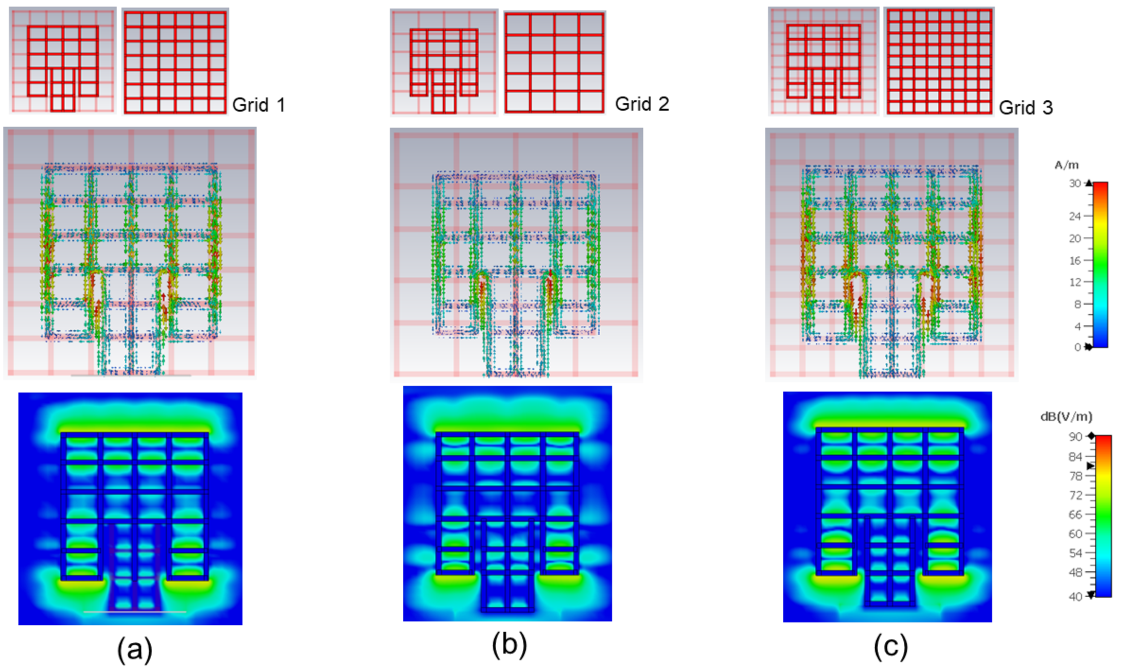

Figure 7. Surface current distribution (top) and ∣Ey∣ field amplitude (lower) at f = 2.6 GHz for three types of meshed ground plane (gpx = gpy = 64.4 mm, h = 3 mm, t = 1 mm, d = 1.5 mm, q = 1.9 mm): (**a**) 7 × 8 wire mesh (L = M = 45.2 mm and n = 16.3 mm); (**b**) 5 × 6 wire mesh (L = M = 42.4 mm and n = 16.2 mm); (**c**) 9 × 10 wire mesh (L = M = 45.5 mm and n = 16.3 mm).

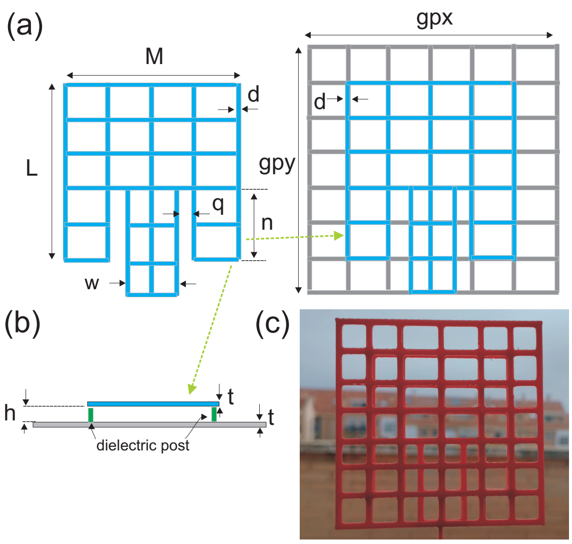

Figure 8. Scheme of the proposed configuration for the semitransparent patch: (**a**) mesh patch layer (**left**) and the patch overlaid on the ground plane (**right**); (**b**) side view of the antenna's metal layers without a substrate; (**c**) back-view photo of a prototype to illustrate transparency.

It is clear that once we set the mesh design for both the patch and ground plane, we can change the antenna's operating frequency by adjusting the patch size and tweaking the microstrip line's position using the inset. The graph in Figure 9 shows how the antenna's response varies depending on the patch size. For a patch measuring L = M = 46.2 mm, the antenna sits right at the target frequency of f = 2.6 GHz, with an impedance bandwidth ($|S_{11}| < -10$ dB) of 2.7%. At this frequency, the antenna size with this mesh setup is $0.4\lambda_0$, which is smaller than expected for a continuous patch. In these antennas, it is known that as the transparency increases (meaning the grid becomes less dense), the resonance frequency shifts to lower values. To maintain a specific operating range, we shrank the patch size as we increased transparency. This was evidenced in the values obtained for the antenna size as the grid became more transparent (Figure 4).

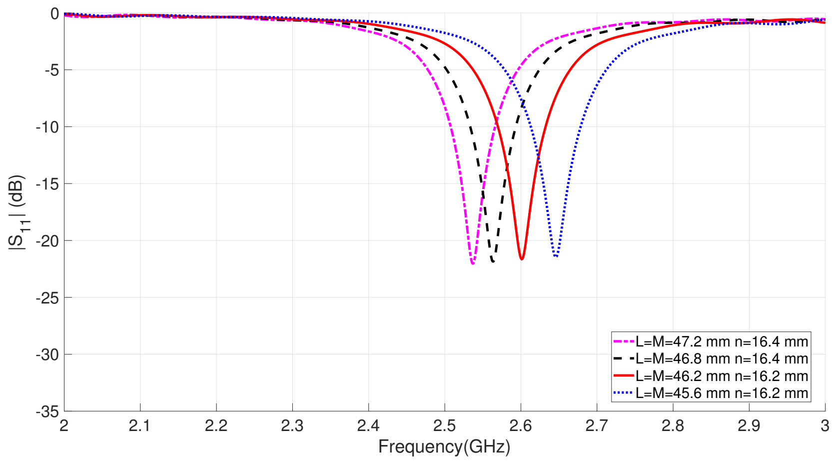

Figure 9. Simulated impedance response (S_{11}) of the proposed antenna for different sizes of the square patch considering the ground plane with 7 × 8 wire mesh, i.e., grid 1 (gpx = gpy = 64.4 mm, h = 3 mm, t = 1 mm, d = 2 mm, q = 1.9 mm, and w = 15.6 mm).

One last crucial aspect to explore in this section is the size of the metallic wires composing the antenna mesh. For simplicity, we assume that they are all uniform. Starting with wire thickness, taking into account the conductivity of silver, and assuming the conductor approximation described in Equation (2) (where f represents frequency and μ_0 stands for the permeability of free space and assuming $\mu_r = 1$ for the relative permeability of the conductor), we can calculate the skin depth at the antenna's operating frequency of f = 2.6 GHz.

$$\delta_s = \sqrt{\frac{1}{\pi f \mu_0 \sigma}} \approx 9.87 \times 10^{-3} \sqrt{\frac{1}{\sigma}} \tag{2}$$

In this scenario, where $\delta_s = 1.25$ µm, we observe that the distance at which the field concentrates does not impose restrictions on the thickness of the wire layers. Although the wire thickness minimally affects the antenna's response, its value is governed by mechanical requirements. As the antenna lacks a substrate and is 3D-printed using plastic materials, the wire thickness (denoted as 'd') must provide adequate mechanical stability and rigidity for suspension and placement in the window or final location. Printer tests indicated significantly improved rigidity for thicknesses above 0.8 mm. Therefore, for safety margins, a value of t = 1 mm was chosen throughout the research.

To understand the effect of metallic wire width on the antenna's impedance response, Figure 10 depicts the variation in S_{11} for three different widths (d). It is evident from the antenna's response that as the wire width decreases, the resonance shifts to lower frequencies, necessitating a smaller antenna to adjust its frequency. Naturally, a thinner 'd' would enhance transparency if maintaining the antenna's size. However, as the patch size decreases, this effect would be partially or wholly offset, depending on the 'd' variation.

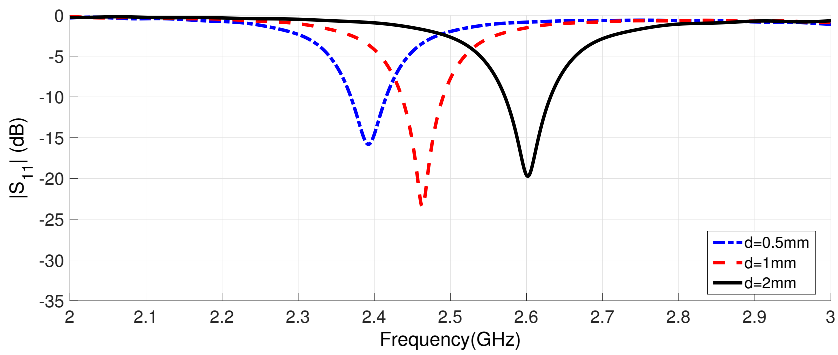

Figure 10. Simulated impedance response (S_{11}) of the proposed antenna for different widths (d) of mesh wires (L = M = 46.2 mm, gpx = gpy = 64.4 mm, h = 3 mm, t = 1 mm, n = 16.3 mm, q = 1.9 mm, and w = 15.6 mm).

Further exploring the impact of wire width on antenna gain, Figure 11 displays the antenna's broadside gain for the same 'd' values as depicted in Figure 10. Reducing the wire width notably diminishes the antenna's primary performance, decreasing from a maximum gain of 8.5 dB to 7.9 dB and 7.6 dB for d = 2 mm, d = 1 mm, and d = 0.5 mm, respectively. The maximum gain curves depicted in Figure 11 shift towards the left as the wire width decreases, which is consistent with the trend observed in the return losses shown in Figure 10.

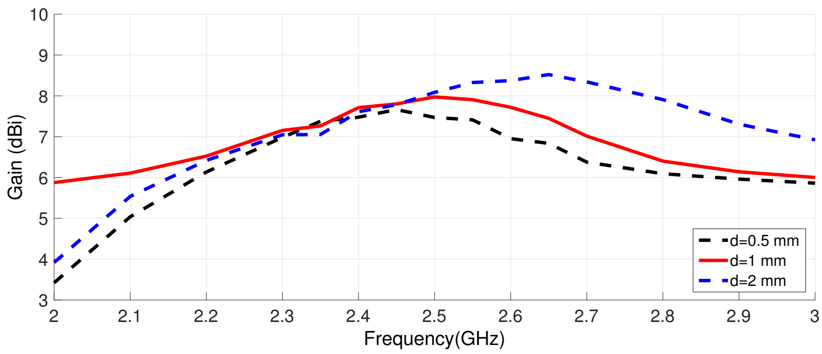

Figure 11. Simulated gain of the proposed antenna for different widths (d) of mesh wires (L = M = 46.2 mm, gpx = gpy = 64.4 mm, h = 3 mm, t = 1 mm, n = 16.3 mm, q = 1.9 mm, and w = 15.6 mm).

Considering the minor effect on transparency, the optimal choice to maintain the patch's efficiency as a radiator is not to significantly reduce 'd'; instead, opting for a value within the previously simulated higher range, i.e., d = 2 mm, seems more advantageous.

Table 1 indicates the values for the main geometric parameters for the designed semitransparent patch antenna. Numerical analysis suggests promising performance, with achieved gains exceeding 8 dB; good impedance matching within an FBW of 2.5–3%; and radiation patterns, FTB ratios, and cross polarizations similar to those of a non-transparent continuous patch.

Table 1. Parameters of the semitransparent patch antenna.

Parameter	L	M	gpx	gpy	h
value (mm)	46.2	46.2	64.4	64.4	3
Parameter	t	d	q	n	w
value (mm)	1	2	1.9	16.3	15.6

In the following section, we evaluate the performance achieved by our cost-effective design.

3. Performance Evaluation of the Antenna

This section details the manufacturing of prototypes, characterizes the final result of the printed and metallized parts of the proposed antenna using microscopy images, and analyzes the impact of the metallized surface on the performance of the semitransparent patch through simulation.

3.1. 3D Printing Low-Cost Fabrication

3D printing has revolutionized modern manufacturing by offering an innovative and versatile technique for creating three-dimensional objects from digital models. This is illustrated in Figure 12, where one of the semitransparent antenna models can be seen in Figure 12a, along with the result of printing semitransparent patch prototypes using different non-metallized materials in Figure 12b,c,d. This technique stands out for its relatively low cost compared to traditional manufacturing methods [37,38], as it minimizes material waste by building objects layer by layer, using only the precise amount of material required. Furthermore, 3D printing showcases an impressive diversity of available materials, ranging from plastics and resins to metals, ceramics, and even biodegradable materials, significantly expanding RF design possibilities and applications [39].

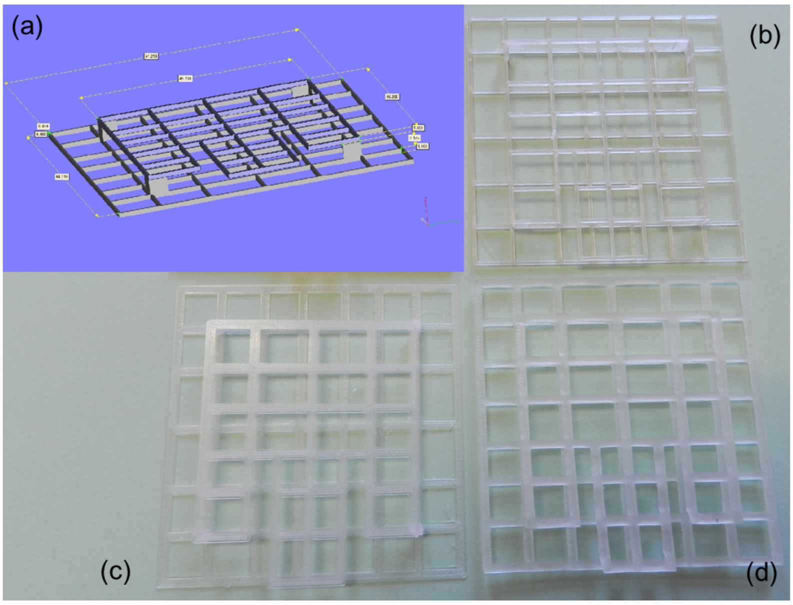

Figure 12. Illustrative stages of the 3D manufacturing process for the antenna: (**a**) model used for printing; (**b**) PETG prototype manufactured with d = 0.5 mm and t = 1 mm; (**c**) PETG prototype manufactured with d = 2 mm and t = 0.4 mm; (**d**) resin prototype manufactured with d = 2 mm and t = 1 mm.

From an antenna perspective, an issue that remains unresolved is the metallization of printed surfaces. On one hand, there is the possibility of printing using FDM diffusion techniques employing metallic filaments [39]. However, the final conductivity of presently accessible materials falls short, and published outcomes have been inefficient. Additional methodologies, such as metal diffusion or the utilization of conductive filament in conjunction with subsequent electroplating or electrodeposition, represent more advanced alternatives. However, these methods come with higher costs and limited accessibility in contrast to the approach expounded upon in this article. In our case, we chose to print using dielectric filaments (primarily PLA, PET, and ABS) and later metallize the surfaces using silver conductive paint (SCP). There is a wide range of manufacturing techniques and numerous dielectric materials available to carry out these printing processes, as detailed comprehensively in [40], the authors of which provide detailed information regarding the ranges they offer for tolerances in objects and, more importantly, their impact on surface quality. Surface quality, in our case, affects the surface roughness level, which, alongside the conductivity of the metal layer covering the antenna's metallized elements, is the primary determinant of the patch's electrical performance.

The surface roughness in transmission lines impacts both losses and signal phase delay [41]. Consequently, patch antenna simulations often underestimate losses stemming from surface roughness, which is significant in our case due to the inherent inevitability of roughness in 3D printing. Assuming surface roughness as a random process, advanced models have recently been proposed to address this problem. In a physical approach with a clear practical focus aimed at simulation designs, the gradient model was proposed in [42]. This model calculates a conductivity gradient (perpendicular to the surface) based on the surface parameter (R_q), from which it derives a surface impedance, enhancing loss estimation. Additionally, it enables a more precise modeling of propagation delay in transmission lines or downshift of resonance frequencies in resonators [43]. R_q, known as the root mean square of measured microscopic peaks and valleys, given a roughness profile ($z(x)$) and its length (l_e), is determined according to

$$R_q = \sqrt{\frac{1}{l_e}\int_0^{l_e} z^2(x)dx} \tag{3}$$

This parameter is employed, in the case of lossy metals, by CST Microwave Studio to quantify the degree of surface roughness and introduce improvements in simulations by modeling surface impedance. To incorporate this effect into simulations and include it in the antenna gain analysis, we require an estimation of the magnitude of roughness on 3D-printed surfaces.

Table 2 details the characteristics of several manufactured prototypes, such as their manufacturing process, materials used, and printing layer thickness. It also indicates where prototype photographs appear, if available. Typical roughness values for these cases compiled from similar materials and thicknesses based on referenced studies are included in the table as R_a parameter ranges measured within this context. It is essential to note that these ranges are broad due to the dependence of surface roughness on multiple factors, including the orientation (deposition) angle [44]. For instance, factors like printing layer thickness, material properties, printing techniques, and printer settings contribute to this variability. In [40], the most significant factors affecting the surface roughness of PLA and ABS were identified, listed in order of importance: layer thickness, build orientation, printing speed, nozzle diameter, and temperature. However, the references consulted and their values included in Table 2 suggest that the roughness of printed plastic (PLA, ABS, and PET) surfaces typically falls between 0.1 and 0.3 times the printing thickness, reaching, at most, the thickness of the layer. To incorporate this effect into simulations using the commonly used R_a experimental parameter, it needs to correlate with the software's characteristic parameter for lossy metals (R_q). R_q represents the average roughness, which is the arithmetic average of the absolute values of the roughness profile ordinates, and is calculated as

$$R_a = \frac{1}{l_e}\int_0^{l_e} |z(x)|dx \tag{4}$$

The relationship between R_q and R_a varies depending on the surface roughness profile ($z(x)$) and may change based on the specific nature of the surface, the measurement technique employed, or the distribution of its irregularities. Generally, R_q tends to be smaller than R_a. It has been observed that R_a can typically exceed R_q by about 10% to 20% [40,44]. Commonly observed associations include R_a = 1.1R_q and R_a = 1.2R_q; therefore, in our case, we consider these parameters as equivalent for the purposes of our qualitative analysis.

Table 2. Characteristic overview of 3D printing prototypes and comparison with the state-of-the-art roughness range (roughness data were extracted for a similar printed layer thickness).

Process	**Material**	**Printed Layer**	**Photo**	**Range R_a (µm)**	**Range R_a (µm)**	**Range R_a (µm)**	**Range R_a (µm)**
AM	Filament	thickness	Figure	ref [40]	ref [44]	ref [45]	ref [46]
FDM	PLA	0.12 mm	Figure 13	5–10	-	6–22	-
FDM	ABS	-	-	6–15	11–18	-	7–20
FDM	PET	0.1 mm	Figure 12b,c	4–31	-	-	-
SLA/DLP	E-guard (resin)	0.1 mm	Figure 12d	5–30	-	-	-

Conductive paints and inks typically exhibit lower conductivity compared to the bulk material they contain [39]. Nevertheless, metallization using SCP has been successfully employed over the antenna in previous RF designs using methods such as airbrushing, paint-gun application, or manual brush application [37,38,47]. In this work, the antenna was hand-painted with a brush, applying a single layer on both sides of the conductive parts of the patch previously printed with dielectric filament. The paint was a commercial SCP containing approximately 40–50% silver by weight, along with other solvents, such as ethanol and acetone, as its main components [48]. Figure 13a depicts the 3D-printed parts of the antenna, patch, and ground plane in unpainted PLA, along with the paint used. The non-uniform configurations of the meshes for the ground plane and the patch, allowing them to visually overlap for improved transparency, are also detailed in Figure 13a. The final result of the antenna after paint application and assembly with adhesive is shown in Figure 13b. Obviously, soldering the connector is not feasible; hence, it is mounted onto the antenna using silver epoxy. The metallic paint used for manual metallization in some literature examples exhibits variable conductivity based on its composition and application. For instance, in [47], a stretchable silver conductive paste was used, yielding a conductivity value of $\sigma = 1.7 \times 10^4$ S/m for a paste layer with a thickness of 26.5 µm. Another hand-painted design is described in [38], where it was concluded that the manufacturer's nominal conductivity of the paint ($\sigma = 1.3 \times 10^6$ S/m) did not significantly impact the antenna's efficiency in the measurement. However, the surface layer's conductivity was not experimentally characterized. In [37], similar SCP as in our case [48] was used to airbrush a 3D-printed filter prototype. Subsequently, in this study, the metallization was enhanced through an electroplating process, but before this, the estimated paint layer, with a thickness ranging between 10 and 20 µm, was experimentally characterized. Resistance was measured using probes at different distances across the dry paint layer, resulting in a DC conductivity value between $\sigma = 2.86 \times 10^5$ S/m and $\sigma = 5.7 \times 10^5$ S/m. This value might serve as a reasonable estimation for the conductivity range of our hand-painted surface for the metallic mesh.

Hand painting allows for greater control of strokes and details, resulting in a visible texture and brush marks on the surface, as can be seen in Figure 14. The paint was carefully applied, aiming for uniformity and complete coverage of the dielectric material surface. Figure 14a shows the detail of a semitransparent antenna prototype with a wire width of d = 1 mm in the center. For comparison, two prototypes are placed beside it; the thicker one on the left has a width of d = 2 mm, and the thinner one on the right has width of d = 0.5 mm. Transparency above 60% was achieved in all cases, with slightly higher values for prototypes with thinner wires. The result of the printing and metallization process appears reasonable at first sight, although slight brush marks and the roughness of the printed material persist, as shown in the detailed photos in Figure 14b,c. In the following section, we analyze the surface quality in greater detail using microscopic view analysis.

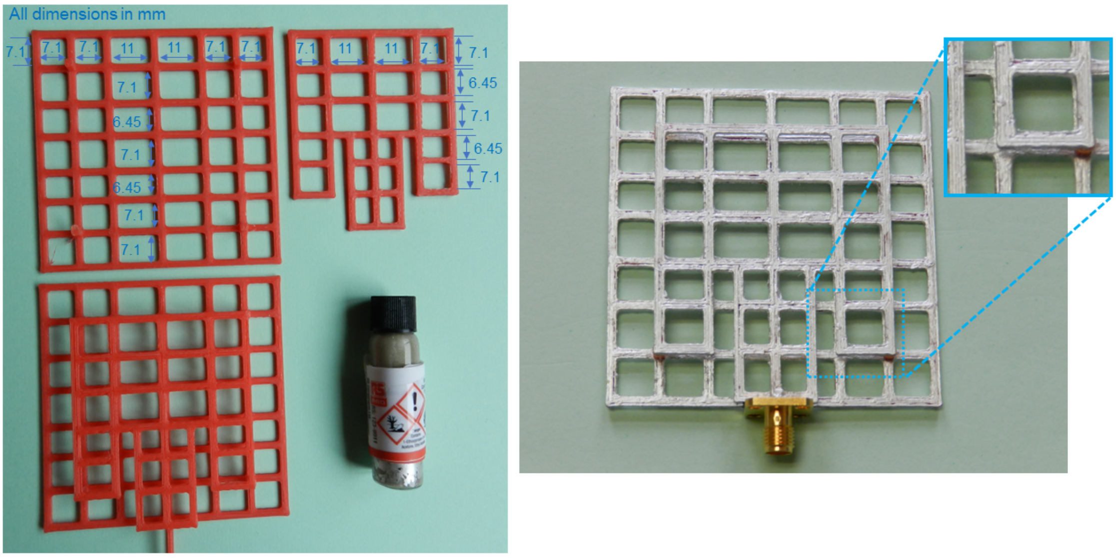

(a) (b)

Figure 13. Photograph of the manufactured mesh antenna prototype: (**a**) 3D-printed PLA parts without metallization and the applied conductive paint (SCP), along with details depicting the non-uniform separation of the grid wires; (**b**) antenna metallized using the SCP and incorporating the SMA connector.

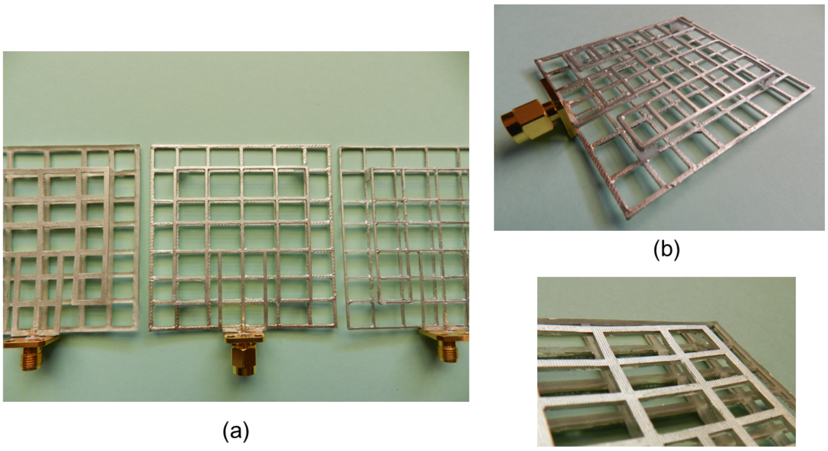

(a) (b) (c)

Figure 14. Photographs of manufactured prototypes. (**a**) With resin and a width of d = 2 mm (**left**); PET and a width of d = 1 mm (**center**); and PET and a width of d = 0.5 mm (**right**). (**b**) Perspective view of the mesh patch (PET and a width of d = 1mm). (**c**) Surface detail (resin and a width of d = 2 mm).

3.2. Microscopic Characterization

We now describe the hand-painted surface of the two manufactured prototypes using a scanning electron microscope (SEM). Although the photographs presented Section 3.1 showed a uniformly painted surface at first glance, at the microscopic level, in Figure 15, we observe the roughness and small irregularities present on the surface of the 3D-printed material. Figure 15a,b display the prototype manufactured in PET using FDM with a width of $d = 1$ mm. In this case, small longitudinal grooves, paint burrs at the corners, and thin paint filaments protruding from the grid structure are evident. Another prototype, the resin antenna manufactured using SLA with a width of $d = 2$ mm, is shown unpainted in Figure 12d. Figure 15c displays its surface, showing significant structural roughness in the transverse direction of the printed wires. The distance between peaks and valleys is clearly visible in Figure 15d, and although it was not quantified, it is observed to be significant compared to the width of the wires in the section. The SCP layer microscopically exhibits a fairly regular granular appearance of silver particles, although changes in particle density are evident in Figure 15b,d, with areas changing color due to the absence of silver. Irregularities in the 3D-printed surface due to the filament—not the paint—are also visible in Figure 15c.

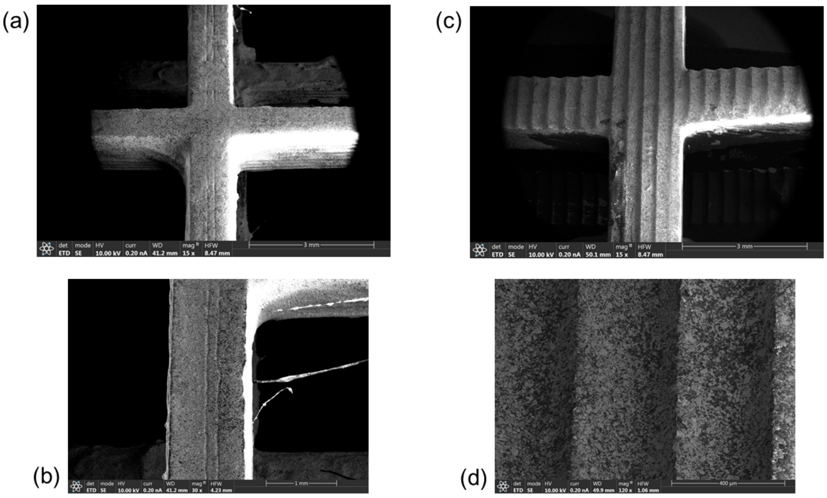

Figure 15. SEM images of two antenna prototypes. (**a**) Detail of a wire crossing printed with PET and a width of d = 1 mm; (**b**) zoomed-in view of a wire printed with PET and a width of d = 1 mm. (**c**) Detail of a wire crossing printed with resin and a width of d = 2 mm; (**d**) zoomed-in view of a wire printed with resin and a width of d = 2 mm.

In the literature, numerous studies have been conducted on the surface characteristics and properties of silver paint or ink. For instance, the authors of [49] delved into the mechanical and conductive properties of silver paint for applications in textile electronics, while the electrical and morphological properties of a hand-painted electrode using silver nanowires are described in [50]. Once applied, silver paint can undergo a thermal curing process, as exemplified in [47], where a sample was subjected to a 110 °C temperature for 15 min. The curing and sintering processes of metal powder or paint substantially enhance the final conductivity of the metallized surface. However, the process temperature limits the use of plastic materials—particularly low-cost materials—in 3D printing of the structure to be metallized [49]. In our case, the paint was air-dried at room temperature, which evidently limited the final outcome. Silver in the paint is commonly found in the form of small particles or colloidal suspensions, and temperature influences the formation of silver flakes due to the chemical reaction between its components. SEM images presented in Figure 16 depict the formation of silver flakes on the surfaces of both prototypes, stratifying to form the paint layer. The size of these flakes varies; in Figure 16a, the detail shows sizes ranging from 2–3 µm up to 15–20 µm. This morphological analysis of the surface demonstrates continuity through the contact of these flakes, which facilitates current transport across the surface. Nonetheless, manual application of the paint and the absence of curing reduce the aggregation of silver flakes, leading to a decrease in the effective conductivity of the surface [49]. In Figure 16c, areas with a lower density of silver particles are uniformly distributed. Additionally, in Figure 16a, some particle aggregates are surrounded by areas not covered by paint, forming islands that decrease metal connectivity, thereby negatively impacting electron transport and effective conductivity [51]. Figure 16b illustrates the basic chemical composition analysis of the two marked areas comprising the silver island: one with a high silver content (Ag) and the other with compounds from the material used for 3D printing (for example, O or C). Finally, in Figure 16d, the irregular coating applied by by the brush at the interface between two differently elevated zones on the surface is visible. These irregularities stem from the hand-painting process with a brush, unlike other techniques like airbrushing that achieve greater uniformity.

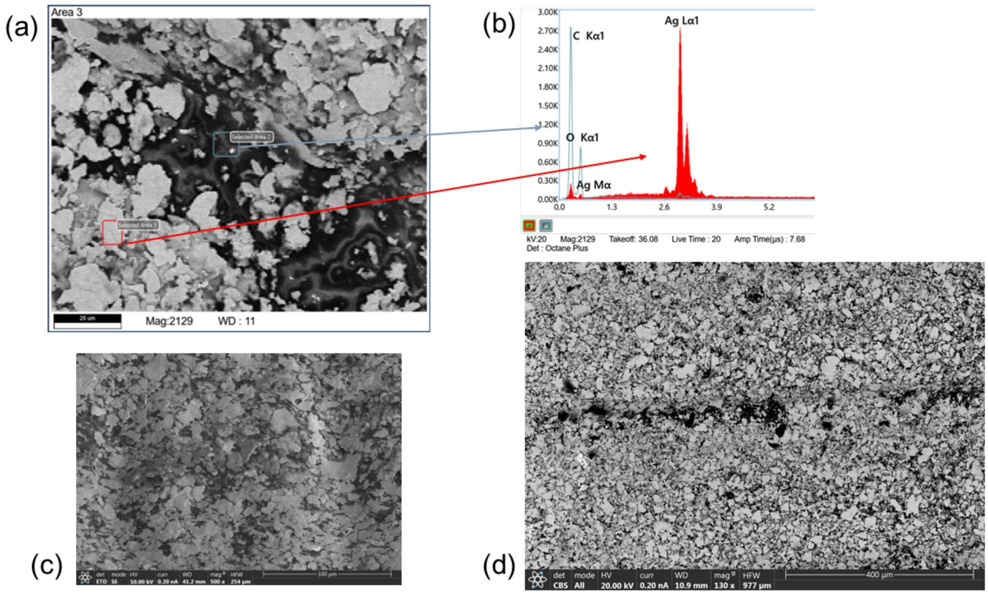

Figure 16. SEM images of the prototypes: (**a**) formation of silver islands with areas lacking a metal layer; (**b**) elemental SEM analysis of material composition; (**c**) silver flakes on the surface; (**d**) non-uniformities in the SCP layer.

Considering these factors, it is reasonable to anticipate a lower conductivity level on the surface compared to the measurement reported in [37]. This is attributed to both the brush application and the observed lack of connectivity in the SEM images of the surface. Starting from the approximate values measured in [37] ($\sigma = 2.8 - 5.7 \times 10^5$ S/m), establishing an upper limit, it seems reasonable to incorporate lower conductivity values into our numerical analysis of the antenna. Therefore, broad range of conductivity values between $\sigma = 5 \times 10^5$ S/m and $\sigma = 1 \times 10^4$ S/m is considered. In the subsequent section, we explore the impact on the antenna parameters by integrating the electrical characteristics and the degree of surface roughness into the simulation model.

3.3. Antenna Response Analysis: Surface Roughness and Conductivity

Figure 17 illustrates the simulated radiation efficiency for the proposed antenna concerning frequency, considering various conductivities and levels of roughness. The efficiency achieved with ideal smooth metal (upper continuous traces) shows values above 95% in the antenna's frequency range of interest (2.5–2.7 GHz) for $\sigma = 6.3 \times 10^7$ S/m (in blue), which represents the ideal limit for silver. However, reducing conductivity to more realistic values within the measured range [37] results in a drop in the antenna's efficiency drops to around 85% for $\sigma = 5 \times 10^5$ S/m (in red). Introducing different degrees of roughness alongside decreased conductivity significantly reduces the antenna efficiency. For a conductivity of $\sigma = 5 \times 10^5$ S/m, with roughness values (Rq) of 10 µm, 25 µm, 50 µm, and 100 µm, radiation efficiencies of 78.6%, 64.5%, 49.7%, and 36% are obtained, respectively. These Rq values correspond to 0.1, 0.25, 0.5, and 1 times the thickness of the printed layer. This range aligns with observed values in the state of the art for low-cost 3D-printed materials like PLA, ABS, and PET, including the absolute thickness limit of the printed layer [40]. In our case, we found that in contrast to maximum height, the distance between valleys and peaks is much less than 0.5 of the printed layer thickness for FDM with PET and of that order, at most, for the SLA-manufactured resin prototype. Therefore, considering the surface is smoothed by the SCP layer, the roughness in terms of R_a or R_q

should be significantly lower—approximately within 0.1 times the layer thickness for the 3D-printed dielectric material. However, in our case, there exists the inherent roughness of the silver flake layer, which, although not continuous, exhibits irregularities of that magnitude, as observed in Figure 16.

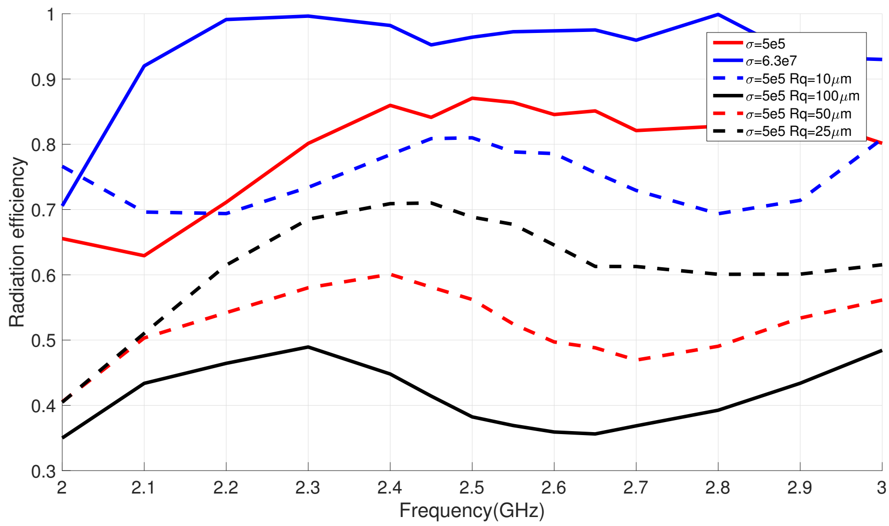

Figure 17. Simulated radiation efficiency calculated as a function of the conductivity of the metallic material of the antenna and the roughness of the surface: (smooth surfaces in continuous trace at the top of the figure) (L = M = 46.2 mm, gpx = gpy = 64.4 mm, h = 3 mm, t = 1 mm, n = 16.3 mm, q = 1.9 mm, and w = 15.6 mm).

To analyze the impact of surface roughness on impedance matching of the antenna, Figure 18 presents the simulated S_{11} parameter for the same roughness parameter (Rq) values. For the simulations, a conductivity of $\sigma = 5 \times 10^5$ S/m was selected, which falls within the likely range of values measured for this type of metallic ink [37]. This level of conductivity is sufficiently high to disregard dielectric and polarization effects, ensuring the continued validity of the approximation provided by Equation (2) [52]. According to this expression, the skin depth in this case is $\delta_s = 14$ μm, aligning with typical thicknesses for this type of metallic ink [37,38,47]. The antenna is well matched for smooth cases and for Rq values below 25 μm. The figure demonstrates the shift towards lower frequencies in the antenna's operating band as the degree of roughness (Rq) increases [41].

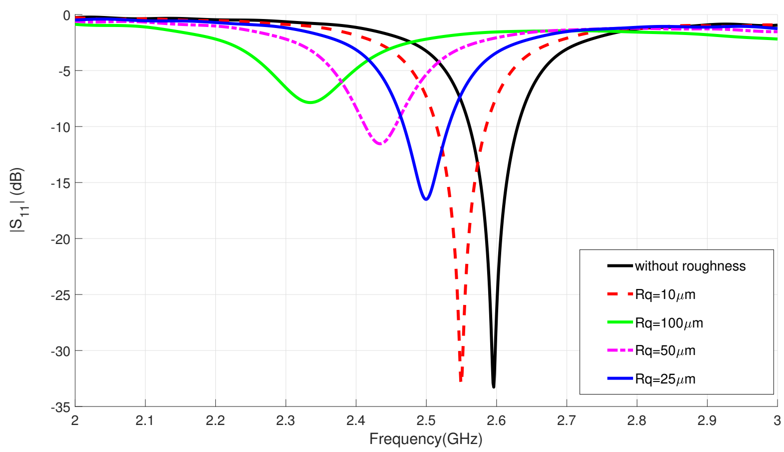

Figure 18. Simulated impedance response (S_{11}) of the proposed antenna for different surface roughness values of metallic material with a conductivity of $\sigma = 5 \times 10^5$ S/m.

Finally, Figure 19 includes the proposed antenna's gain vs. frequency across the entire range of conductivities and three roughness values, extending to the lowest surface print quality level at $Rq = 50$ µm. The combined effect of reduced conductivity and increased roughness significantly impacts the antenna's performance, reducing its theoretical gain. On one hand, the a conductivity decrease by two orders of magnitude results in a reduction in antenna gain from 7.6 dBi, 6.8 dBi, and 5.9 dBi for $Rq = 10$ µm, $Rq = 25$ µm, and $Rq = 50$ µm to 6 dBi, 5.5 dBi, and 4.6 dBi, respectively. On the other hand, increased Rq at all conductivities also leads to reduced antenna gain. For instance, there is a reduction from 7.1 dBi for $\sigma = 5 \times 10^5$ S/m and $Rq = 10$ µm to 5.5 dBi for the same conductivity with $Rq = 50$ µm. Moreover, this rise in roughness in simulations causes a shift in the frequency of the antenna's maximum gain towards lower frequencies. It is evident that controlling the final quality of the 3D-printed surface, particularly by limiting R_a and ensuring sufficient effective conductivity, is critical in achieving a high gain in semitransparent mesh antennas.

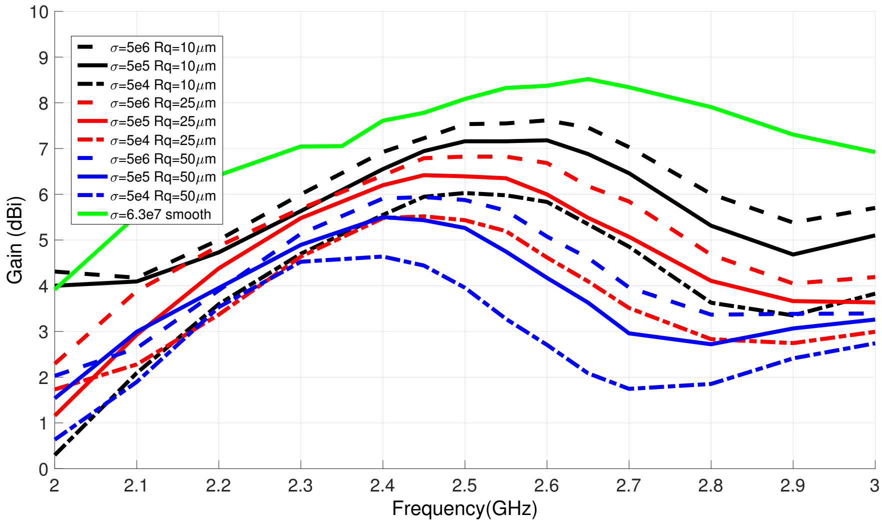

Figure 19. Simulated gain for the semitransparent antenna under different values of conductivity and roughness of the metal surface.

4. Results and Discussion

4.1. Experimental Results

To verify the performance of the proposed antenna with the parameters listed in Table 1, its impedance response and gain were measured in an anechoic chamber. Figure 20 presents a comparison between the experimentally observed realized gain and simulations for different surface conductivity and roughness values. Meanwhile, both simulation and measurement results for impedance matching are included in Figure 21. The measured antenna exhibits an operational frequency centered at $f_c = 2.64$ GHz, with a bandwidth of $|S_{11}| < -10$ dB of 2.7%. Simulated matching curves show good agreement with the measurement for smooth cases (with ideal conductivity and with the conductivity measured in [37]), as well as for cases with low roughness ($R_q = 10$ µm and $R_q = 5$ µm) and high conductivity ($\sigma = 5 \times 10^5$ S/m and $\sigma = 1 \times 10^5$ S/m). For higher roughness values or for low roughness combined with lower conductivities, the simulated response reduces its matching and shifts towards lower frequencies. Regarding the gain, the proposed antenna reaches a peak of 5.4 dBi at a frequency of 2.64 GHz. It can be stated that the comparison of the measurement aligns well with the levels and responses of simulations for lower material conductivity values ($\sigma = 5 \times 10^5$ S/m and $\sigma = 1 \times 10^5$ S/m) and low roughness levels around $R_q = 10$ µm.

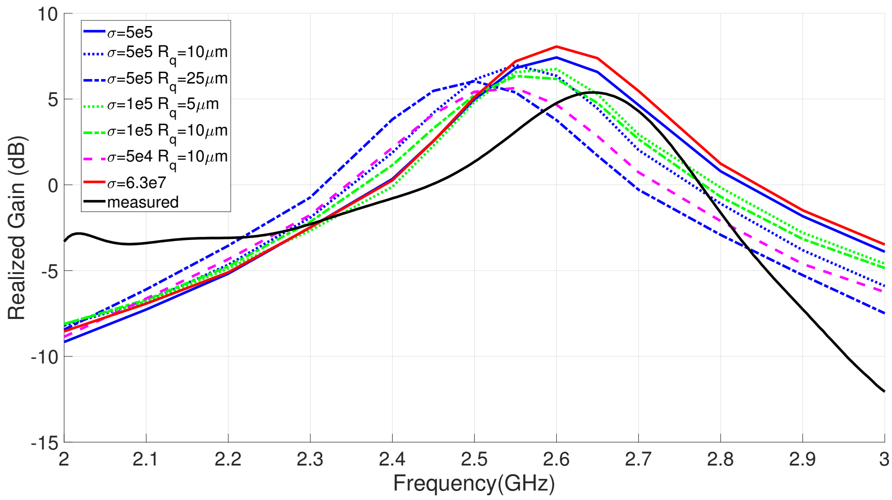

Figure 20. Realized gain for the manufactured semitransparent mesh antenna and for simulations accounts for various conductivity and surface roughness values on the metallic surfaces (L = M = 46.2 mm, gpx = gpy = 64.4 mm, h = 3 mm, t = 1 mm, n = 16.3 mm, q = 1.9 mm, and w = 15.6 mm).

Table 3 presents a summary comparing the impedance, radiation efficiency, and realized gain results. Considering the cost-effectiveness of the 3D printing manufacturing process, the antenna's mesh components were metallized by hand-painting with a brush, and metallic adhesive was used for connector attachment, showcasing satisfactory performance in terms of S_{11} and realized gain for the proposed semitransparent patch. The calculated optical transparency derived from Equation (1) for the antenna with d = 2 mm exceeds 60%. This transparency result is depicted in the accompanying photographs included in Figure 22.

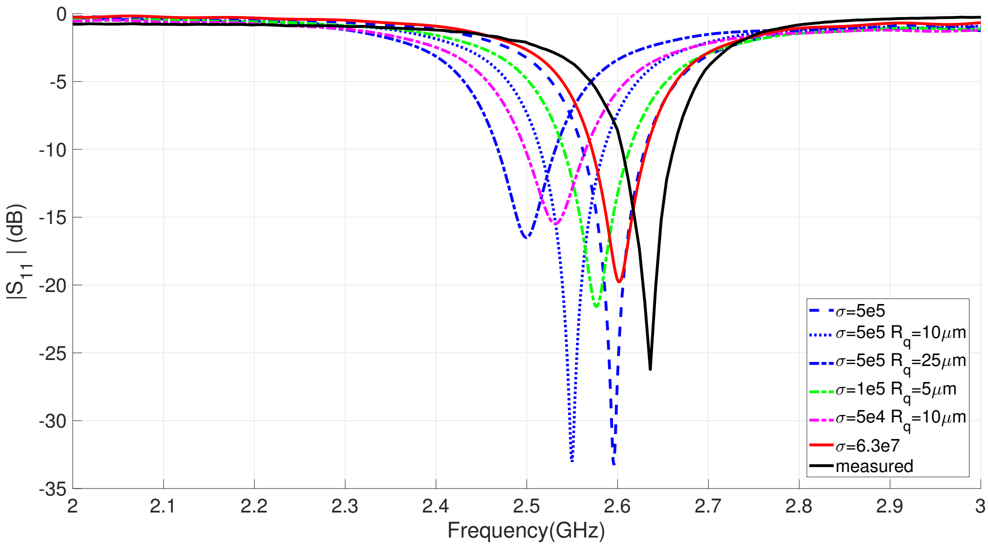

Figure 21. $|S_{11}|$ for the manufactured semitransparent mesh antenna and for simulations accounts for various conductivity and surface roughness values on the metallic surfaces (L = M = 46.2 mm, gpx = gpy = 64.4 mm, h = 3 mm, t = 1 mm, n = 16.3 mm, q = 1.9 mm, and w = 15.6 mm).

Table 3. Semitransparent antenna performance comparison between simulated and measured results.

Case	**Material**			**Impedance BW**			**Radiation**		
Model	**σ (S/m)**	**Rough. Rq μm**	**f_c (GHz)**	**RL (10dB)**	**RL (6dB)**	**f_r (GHz)**	**Peak R.Gain (dB)**	**3 dB BW%**	**rad. eff**
sim lossy	6.3e7	smooth	2.6	2.31%	4%	2.605	8	8.8%	98.2%
sim lossy	5e5	smooth	2.6	2.7%	4.8%	2.6	7.4	8.1%	84.5%
sim lossy	5e5	10	2.55	2.74%	4.7%	2.55	7	8.6%	78.6%
sim lossy	5e5	25	2.5	2.52%	4.6%	2.5	6.1	8.7%	64.5%
sim lossy	1e5	5	2.57	2.9%	5%	2.56	6.3	8.6%	70.7%
sim lossy	5e4	10	2.53	2.4%	5.1%	2.58	5.6	6.2%	59.7%
mea PET + SCP	-	-	2.64	2.7%	3.9%	2.64	5.4	7.6%	-

4.2. Discussion

This study demonstrates the feasibility of designing an antenna with high optical transparency, as shown in Figure 22, utilizing 3D printing for its structure and applying low-cost techniques and materials for fabrication and metallization. Measurements of the proposed mesh patch antenna showcase its favorable performance relative to similar antennas, as detailed in Table 4. This research highlights the potential for advanced designs and applications in sub-6GHz bands for 5G/6G, allowing for integration in windows and glass surfaces without the limitations of surface restrictions or element count, presenting advantages in various RF systems within urban environments, such as improved gain, beamforming capabilities, MIMO arrays, etc.

(a) (b)

Figure 22. Photographs of prototypes placed on a window to showcase their transparency, manufactured with: (**a**) PET and widths of d = 0.5 mm (**left**) and d = 1 mm (**center**); with resin and a width of d = 2 mm (**right**); (**b**) PLA and a width of d = 2 mm (**left**); and PET and a width of d = 0.5 mm (**right**).

Outlined below are some of the advantages offered by these cost-effective antennas:

1. The antenna's design allows for the passage of most visible light, harnessing natural light and minimizing visual impact.
2. The absence of a substrate enables manufacturing using various 3D printing materials, avoiding electrical losses inherent in substrates, reducing economic costs, and eliminating waste and recycling expenses. Furthermore, the lack of a substrate facilitates airflow, potentially lessening wind load or enhancing cooling.
3. The choice of 3D printing material for the antenna, whether metallic for optimized radiation efficiency or as a structural component later metallized with a low-cost dielectric, depends on factors such as material sustainability and recyclability. For

instance, PLA filament sourced from renewable sources like corn starch or sugarcane is considered more environmentally friendly than ABS derived from non-biodegradable fossil fuels [40].

4. The antenna's construction involves meshing its metallic parts, significantly reducing material usage and coupled with the absence of a substrate, implementing a mass reduction technique that drastically decreases its weight, aligning with current research trends [53].
5. The 3D printing technique enables consideration of material and electrical properties as additional parameters in the structure's design. This facilitates the elimination of conductive parts from ground planes, reducing mutual coupling, which is a substantial advantage in MIMO implementations [33].

In this research, we systematically evaluated the impact of the design and manufacturing process on antenna performance, particularly focusing on the surface quality of 3D-printed parts and low-cost metallic coatings (using paint or ink). The results indicate that despite cost limitations, the performance of the semitransparent antenna remains compatible with demanding applications in frequency bands below 6 GHz. However, due to limitations of metallized wires (width, surface quality, and manufacturing), obtaining antennas with both good performance and transparency greater than 50% above these frequencies is challenging. With the hand-painting method used in this work, it was observed that reducing the width of the wires to values below 1.25 mm rapidly affected the matching and gain of the manufactured prototypes, deteriorating their performance. Enhancing the smoothness and conductivity of printed surfaces, potentially through electroplating processes, could yield comparable gains to metallic PCB-based patches, even in designs at frequencies exceeding 10 GHz. A limited increase in transparency is also feasible by reducing the width of the metallic wires if effective conductivity is increased and the quality of 3D-printed surfaces is enhanced. Finally, it is important to note that when conductivity values are below $\sigma = 1 \times 10^5$ S/m, the skin depths obtained from Equation (2) exceed 30 µm, typically surpassing the thickness of the metallic paint layers. As a result, the electric field would penetrate significantly into the structural material, leading to increased losses, reduced confinement of electric field distributions, and a degradation in symmetry.

Table 4 compares the performance of the proposed semitransparent antenna with that of other state-of-the-art transparent antennas. Most showcased works feature patch designs at frequencies similar to ours, with mesh-based patches discussed in [14,17,54] and a stacked configuration reported in [9]. In [31], a micromesh-based stacked patch achieved the highest gain of 6 dBi among all results, boasting a large 19% impedance bandwidth and 70% transparency. However, the micromesh significantly blurs images, obstructing clear views through it, and it is notably larger than our proposed design. We also compared our design with that proposed in [55], the only non-transparent patch based on mesh but using FR4 substrate on PCB at 2.45 GHz, yielding a gain close to 3 dBi, which is notably lower than our outcome. Some transparent patches incorporate water inside a plastic container, as evidenced in [12], achieving a 4 dBi gain at 2.4 GHz but with larger antenna sizes. Additional radiating elements include a slot in SIW technology , achieving 4.8 dBi at 26.3 GHz [27]; a dipole loaded with a split-ring resonator, gaining 5 dBi at 5 GHz [10]; and a meandering monopole with 75% transparency but only 0.74 dBi gain at 2.44 GHz [15]. Upon reviewing the results, we conclude that the cost-effective semitransparent antenna performs exceptionally well in terms of high gain. While its impedance bandwidth is limited compared to other non-patch-type antennas, it aligns well with frequency-sharing patches. This highlights the feasibility of designing low-cost mesh patch antennas with high transparency and strong electromagnetic performance. Additionally, our design prioritizes low complexity, facilitating sustainability in materials and enhancing recyclability.

Table 4. Performance comparison with other reported transparent antennas.

Refs.	Element	Structure/ Substrate	Processing Method	Freq. (GHz)	OT	BW (%)	Gain (dBi)	Size (λ_0^3)	Complexity/ Cost
[17]	Patch	Wire mesh/ ceramic	PCB + cutting	2.73	60-65%	2.2	4.8	0.41 × 0.34	High
[27]	Slot + SIW	TCM /PC	-	26.3	71%	17.3	4.8	1.59 × 1.39 × 0.04	High
[12]	Patch	Water/plexiglass container	CNCM	2.4	-	35	4	2.39 × 2.39 × 0.312	Medium
[9]	Stacked patch	TCM/ PC	-	3.45	70%	39.8	4.1	0.63 × 0.63 × 0.07	High
[31]	Stacked patch	Conductive film /PMM	Metal alloy printing	2.65	70%	19	6	0.88 × 0.88 × 0.08	High
[15]	Meandering monopole	MMF/ glass	SNT	2.44	75%	3.3	0.74	0.34 × 0.34	High
[55]	Patch	Metal mesh Cu/ FR4	PCB	2.45	non OT	4	2.95	-	Low
[54]	Patch	MMF/ acrylic	Phys. deposition	2.45	60%	narrow	2.63	0.41 × 0.41 × 0.008	Medium
[14]	Patch	Micro MM/ acrylic	Phys. deposition	2.44	68.6%	narrow	5.28	-	Medium
[10]	Dipole + split ring	Metal grid/glass	PCB	5	69.8%	64.6	5	0.67 × 0.83 × 0.019	Medium
This work	Patch	Painted mesh/ air	PLA 3D printing+ SCP	2.64	60%	2.7	5.4	0.56 × 0.56 × 0.043	Low

An illustrative image of the solution proposed in this work is included in Figure 23. It exemplifies the potential application of the proposed semitransparent antennas. For this purpose, ideal array factors combined with the designed antenna were obtained using CST Microwave Studio. These radiating systems, the patch, and two arrays of 2 × 2 and 4 × 4 patch elements operating at 2.6 GHz, are placed on the windows of a smart building, as depicted in Figure 23. For each case, the calculated theoretical 3D radiation pattern is shown, obtaining gain values of 7.6 dBi, 12.5 dBi, and 18 dBi for the three systems. The graphic representation in Figure 23 also includes a photograph of the proposed antenna placed on a window, showcasing the achieved transparency.

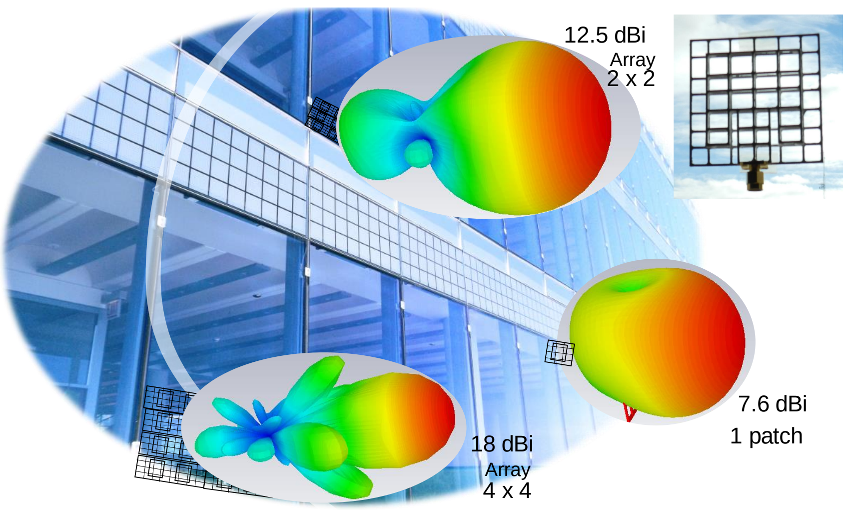

Figure 23. Graphic representation of the proposed application for semitransparent antenna systems. It showcases theoretical 3D radiation patterns for a patch, a 2 × 2 array, a 4 × 4 array, and the manufactured prototype placed on a window.

5. Conclusions

This article introduces a cost-effective method for creating semitransparent antennas suitable for integration into building or vehicle windows. The study presents a substrateless 3D printed mesh patch antenna, achieving a 2.7% bandwidth and a realized gain of 5.4 dBi at 2.6 GHz. This antenna design utilizes any dielectric material for the support structure, eliminating the need for a substrate, and can employ eco-friendly printing materials to reduce the carbon footprint. The impact of the surface roughness and conductivity of the metallic coating on antenna performance was assessed. The performance of the proposed semitransparent antenna reaches levels comparable to those of opaque patches but with 60% transparency in the optical range, allowing for the passage of most light and minimizing visual impact. Furthermore, by foregoing a substrate, the proposed radiating device minimizes losses and costs, optimizes recycling, and offers significant mass reduction. These semitransparent 3D printed meshed antennas are envisioned for sub-6GHz systems utilizing windows in smart buildings, offering advanced 5G/6G urban radio communication infrastructure.

Funding: This research was partially funded by the Spanish State Research Agency under projects PID2022-141055NB-C22 and PDC2022-133811-C22 from MCIN/AEI/10.13039/501100011033.

Institutional Review Board Statement: Not applicable.

Informed Consent Statement: Not applicable.

Data Availability Statement: Data are contained within the article.

Conflicts of Interest: The author declares no conflicts of interest.

Abbreviations

The following abbreviations are used in this manuscript:

ABS	Acrylonitrile butadiene styrene
AgHT	Ag coated polyester
AM	Additive manufacturing
AZO	Aluminum zinc oxide
CNCM	Computer numerical control machining
DLP	Digital (direct) light processing
FDM	Fused deposition modeling
FBW	Fractional bandwidth
FFF	Fused filament fabrication
FTB	Front to back ratio
ITO	Indium tin oxide
IZTO	Indium zinc thin oxide
MIMO	Multiple-input multiple output
MMF	Metal mesh film
OT	Optical transparency
PCB	Printed circuit board
PC	Polycarbonates
PET	Polyethylene terephthalate
PIFA	Planar inverted folded antenna
PLA	Polylactic acid
PMM	Polymethyl methacrylate
PVD	Physical vapor deposition
SCP	Silver conductive paint
SIW	Substrate integrated waveguide
SLS	Selective laser sintering
SLA	Stereolithography
SNT	Self-assembling nanoparticle technology
TCM	Transparent conductive mesh
TCO	Transparent conducting oxides
WMM	Wired metal mesh
ZnO	Doped zinc oxide

References

1. Bariah, L.; Mohjazi, L.; Muhaidat, S.; Sofotasios, P.C.; Kurt, G.K.; Yanikomeroglu, H.; Dobre, O.A. A Prospective Look: Key Enabling Technologies, Applications and Open Research Topics in 6G Networks. *IEEE Access* **2020**, *8*, 174792–174820. [CrossRef]
2. López, O.L.A.; Alves, H.; Souza, R.D.; Montejo-Sánchez, S.; Fernández, E.M.G.; Latva-Aho, M. Massive Wireless Energy Transfer: Enabling Sustainable IoT Toward 6G Era. *IEEE Internet Things J.* **2021**, *8*, 8816–8835. [CrossRef]
3. Ikram, M.; Sultan, K.; Lateef, M.F.; Alqadami, A.S.M. A Road towards 6G Communication-A Review of 5G Antennas, Arrays, and Wearable Devices. *Electronics* **2022**, *11*, 169. [CrossRef]
4. Green, R.B.; Guzman, M.; Izyumskaya, N.; Ullah, B.; Hia, S.; Pitchford, J.; Timsina, R.; Avrutin, V.; Ozgur, U.; Morkoc, H.; et al. Optically Transparent Antennas and Filters: A Smart City Concept to Alleviate Infrastructure and Network Capacity Challenges. *IEEE Antennas Propag. Mag.* **2019**, *61*, 37–47. [CrossRef]
5. Freni, A.; Beccaria, M.; Mazzinghi, A.; Massaccesi, A.; Pirinoli, P. Low-Profile and Low-Visual Impact Smart Electromagnetic Curved Passive Skins for Enhancing Connectivity in Urban Scenarios. *Electronics* **2023**, *12*, 4491. [CrossRef]
6. Silva, Z.J.; Valenta, C.R.; Durgin, G.D. Optically Transparent Antennas: A Survey of Transparent Microwave Conductor Performance and Applications. *IEEE Antennas Propag. Mag.* **2021**, *63*, 27–39. [CrossRef]
7. Fang, X.S.; Leung, K.W. Design of Wideband Omnidirectional Two-Layer Transparent Hemispherical Dielectric Resonator Antenna. *IEEE Trans. Antennas Propag.* **2014**, *62*, 5353–5357. [CrossRef]
8. Clasen, G.; Langley, R. Meshed patch antennas. *IEEE Trans. Antennas Propag.* **2004**, *52*, 1412–1416. [CrossRef]
9. Shi, Y.; Wang, W.J. A Transparent Wideband Dual-Polarized Antenna for Sub-6 GHz Application. *IEEE Antennas Wirel. Propag. Lett.* **2022**, *21*, 2020–2024. [CrossRef]
10. Sun, Y.X.; Wu, D.; Fang, X.S.; Ren, J. On-Glass Grid Structure and Its Application in Highly-Transparent Antenna for Internet of Vehicles. *IEEE Trans. Veh. Technol.* **2023**, *72*, 93–101. [CrossRef]
11. Sun, J.; Luk, K.M. A Wideband and Optically Transparent Water Patch Antenna With Broadside Radiation Pattern. *IEEE Antennas Wirel. Propag. Lett.* **2020**, *19*, 341–345. [CrossRef]
12. Sun, J.; Luk, K.M. A Wideband Low Cost and Optically Transparent Water Patch Antenna With Omnidirectional Conical Beam Radiation Patterns. *IEEE Trans. Antennas Propag.* **2017**, *65*, 4478–4485. [CrossRef]
13. Saberin, J.R.; Furse, C. Challenges with Optically Transparent Patch Antennas. *IEEE Antennas Propag. Mag.* **2012**, *54*, 10–16. [CrossRef]
14. Kang, S.H.; Jung, C.W. Transparent Patch Antenna Using Metal Mesh. *IEEE Trans. Antennas Propag.* **2018**, *66*, 2095–2100. [CrossRef]
15. Li, Q.L.; Cheung, S.W.; Wu, D.; Yuk, T.I. Optically Transparent Dual-Band MIMO Antenna Using Micro-Metal Mesh Conductive Film for WLAN System. *IEEE Antennas Wirel. Propag. Lett.* **2017**, *16*, 920–923. [CrossRef]
16. Clasen, G.; Langley, R.J. Gridded circular patch antennas. *Microw. Opt. Technol. Lett.* **1999**, *21*, 311–313. [CrossRef]
17. Ryan, C.G.M.; Eleftheriades, G.V. Single- and Dual-Band Transparent Circularly Polarized Patch Antennas with Metamaterial Loading. *IEEE Antennas Wirel. Propag. Lett.* **2015**, *14*, 470–473. [CrossRef]
18. Li, W.; Yarali, E.; Bakytbekov, A.; Anthopoulos, T.D.; Shamim, A. Highly transparent and conductive electrodes enabled by scalable printing-and-sintering of silver nanowires. *Nanotechnology* **2020**, *31*, 395201. [CrossRef]
19. Yao, Y.; Shao, Y.; Zhang, J.; Zhang, J. A Transparent Antenna Using Metal Mesh for UWB MIMO Applications. *IEEE Trans. Antennas Propag.* **2023**, *71*, 3836–3844. [CrossRef]
20. Yazdani, R.; Yousefi, M.; Aliakbarian, H.; Oraizi, H.; Vandenbosch, G.A.E. Miniaturized Triple-Band Highly Transparent Antenna. *IEEE Trans. Antennas Propag.* **2020**, *68*, 712–718. [CrossRef]
21. Xi, B.; Liang, X.; Chen, Q.; Wang, K.; Geng, J.; Jin, R. Optical Transparent Antenna Array Integrated With Solar Cell. *IEEE Antennas Wirel. Propag. Lett.* **2020**, *19*, 457–461. [CrossRef]
22. Yekan, T.; Baktur, R. Conformal Integrated Solar Panel Antennas: Two effective integration methods of antennas with solar cells. *IEEE Antennas Propag. Mag.* **2017**, *59*, 69–78. [CrossRef]
23. Hong, W.; Lim, S.; Ko, S.; Kim, Y.G. Optically Invisible Antenna Integrated Within an OLED Touch Display Panel for IoT Applications. *IEEE Trans. Antennas Propag.* **2017**, *65*, 3750–3755. [CrossRef]
24. Morimoto, Y.; Shiu, S.; Huang, I.W.; Fest, E.; Ye, G.; Zhu, J. Optically Transparent Antenna for Smart Glasses. *IEEE Open J. Antennas Propag.* **2023**, *4*, 159–167. [CrossRef]
25. Wagih, M.; Weddell, A.S.; Beeby, S. Meshed High-Impedance Matching Network-Free Rectenna Optimized for Additive Manufacturing. *IEEE Open J. Antennas Propag.* **2020**, *1*, 615–626. [CrossRef]
26. Lin, Y.M.; Wu, H.W.; Hung, C.Y.; Chang, S.J.; Liu, R. Dual-Polarized Transparent Antenna and Its Application for Capsule Endoscopy System. *Electronics* **2023**, *12*, 3124. [CrossRef]
27. Shi, Y.; Wang, W.J.; Hu, T.T. A Transparent SIW Cavity-Based Millimeter-Wave Slot Antenna for 5G Communication. *IEEE Antennas Wirel. Propag. Lett.* **2022**, *21*, 1105–1109. [CrossRef]
28. Lee, I.G.; Yoon, Y.J.; Choi, K.S.; Hong, I.P. Design of an Optical Transparent Absorber and Defect Diagnostics Analysis Based on Near-Field Measurement. *Sensors* **2021**, *21*, 3076. [CrossRef]
29. Wan, S.; Lu, P.; Yin, D.; Guan, X.; Ni, W. A compact hybrid solar and electromagnetic energy harvester at 2.45 GHz microstrip rectenna. *AEU Int. J. Electron. Commun.* **2023**, *172*, 154941. [CrossRef]

30. Hu, H.T.; Chen, B.J.; Chan, C.H. A Transparent Proximity-Coupled-Fed Patch Antenna With Enhanced Bandwidth and Filtering Response. *IEEE Access* **2021**, *9*, 32774–32780. [CrossRef]
31. Ding, C.; Liu, L.; Luk, K.M. An Optically Transparent Dual-Polarized Stacked Patch Antenna With Metal-Mesh Films. *IEEE Antennas Wirel. Propag. Lett.* **2019**, *18*, 1981–1985. [CrossRef]
32. Fernandez, A.; Touchard, G.; Sanchez, L.I.; Iglesias, E.R. ANTENNA, 2018. EP 3 584 884. Available online: https://data.epo.org/publication-server/document?iDocId=6118369&iFormat=0 (accessed on 26 December 2023).
33. Inclán-Sánchez, L. Analysis of a Semitransparent PIFA Element for MIMO Applications. In Proceedings of the 2022 16th European Conference on Antennas and Propagation (EuCAP), Madrid, Spain, 27 March–1 April 2022; pp. 1–5.
34. Yaqoob, I.; Hashem, I.A.T.; Mehmood, Y.; Gani, A.; Mokhtar, S.; Guizani, S. Enabling Communication Technologies for Smart Cities. *IEEE Commun. Mag.* **2017**, *55*, 112–120. [CrossRef]
35. Medina, W.; Novillo, F.; Chancay, E.; Romero, J. Mechanism to Estimate Effective Spectrum Availability Inside Smart Buildings. *Electronics* **2020**, *9*, 1244. [CrossRef]
36. Rani, S.; Mishra, R.K.; Usman, M.; Kataria, A.; Kumar, P.; Bhambri, P.; Mishra, A.K. Amalgamation of Advanced Technologies for Sustainable Development of Smart City Environment: A Review. *IEEE Access* **2021**, *9*, 150060–150087. [CrossRef]
37. Dionigi, M.; Tomassoni, C.; Venanzoni, G.; Sorrentino, R. Simple High-Performance Metal-Plating Procedure for Stereolithographically 3-D-Printed Waveguide Components. *IEEE Microw. Wirel. Components Lett.* **2017**, *27*, 953–955. [CrossRef]
38. Kuosmanen, M.; Ala-Laurinaho, J.; Holopainen, J.; Viikari, V. Antenna Array Based on 3D-printed Plastic BoR Elements Coated with Conductive Paint. In Proceedings of the 2023 17th European Conference on Antennas and Propagation (EuCAP), Florence, Italy, 26–31 March 2023; pp. 1–5. [CrossRef]
39. Whittaker, T.; Zhang, S.; Powell, A.; Stevens, C.J.; Vardaxoglou, J.Y.C.; Whittow, W. 3D Printing Materials and Techniques for Antennas and Metamaterials: A survey of the latest advances. *IEEE Antennas Propag. Mag.* **2023**, *65*, 10–20. [CrossRef]
40. Golhin, A.P.; Tonello, R.; Frisvad, J.R.; Grammatikos, S.; Strandlie, A. Surface roughness of as-printed polymers: A comprehensive review. *Int. J. Adv. Manuf. Technol.* **2023**, *127*, 987–1043. [CrossRef]
41. Gold, G.; Helmreich, K. A Physical Surface Roughness Model and Its Applications. *IEEE Trans. Microw. Theory Tech.* **2017**, *65*, 3720–3732. [CrossRef]
42. Sepaintner, F.; Scharl, A.; Jakob, J.; Schmalzbauer, M.; Röhrl, F.; Bogner, W.; Zorn, S. An Effective Surface Impedance Concept to Model Arbitrary Roughness Profiles on Printed Circuit Boards up to 110 GHz. *IEEE Microw. Wirel. Technol. Lett.* **2023**, *33*, 783–786. [CrossRef]
43. Gold, G.; Helmreich, K. Surface impedance concept for modeling conductor roughness. In Proceedings of the 2015 IEEE MTT-S International Microwave Symposium, Phoenix, AZ, USA, 17–22 May 2015; pp. 1–4. [CrossRef]
44. Ahn, D.; Kweon, J.H.; Kwon, S.; Song, J.; Lee, S. Representation of surface roughness in fused deposition modeling. *J. Mater. Process. Technol.* **2009**, *209*, 5593–5600. [CrossRef]
45. Yang, L.; Li, S.; Li, Y.; Yang, M.; Yuan, Q. Experimental Investigations for Optimizing the Extrusion Parameters on FDM PLA Printed Parts. *J. Mater. Eng. Perform.* **2019**, *28*, 169–182. [CrossRef]
46. Reddy, V.; Flys, O.; Chaparala, A.; Berrimi, C.E.; V, A.; Rosen, B. Study on surface texture of Fused Deposition Modeling. *Procedia Manuf.* **2018**, *25*, 389–396. [CrossRef]
47. Rizwan, M.; Khan, M.W.A.; Sydänheimo, L.; Virkki, J.; Ukkonen, L. Flexible and Stretchable Brush-Painted Wearable Antenna on a Three-Dimensional (3-D) Printed Substrate. *IEEE Antennas Wirel. Propag. Lett.* **2017**, *16*, 3108–3112. [CrossRef]
48. RS Components. RS Pro Silver Conductive Paint. Available online: https://www.rs-components.com (accessed on 20 September 2023).
49. Zhong, T.; Jin, N.; Yuan, W.; Zhou, C.; Gu, W.; Cui, Z. Printable Stretchable Silver Ink and Application to Printed RFID Tags for Wearable Electronics. *Materials* **2019**, *12*, 3036. [CrossRef] [PubMed]
50. Kim, Y.J.; Kim, G.; Kim, H.K. Study of Brush-Painted Ag Nanowire Network on Flexible Invar Metal Substrate for Curved Thin Film Heater. *Metals* **2019**, *9*, 1073. [CrossRef]
51. Chang, Y.C.; Lu, Y.C.; Hung, Y.J. Controlling the Nanoscale Gaps on Silver Island Film for Efficient Surface-Enhanced Raman Spectroscopy. *Nanomaterials* **2019**, *9*, 470. [CrossRef]
52. Claus, N.; Verhaevert, J.; Rogier, H. Cost-Driven Design of Printed Wideband Antennas with Reduced Silver Ink Consumption for the Internet of Things. *Sensors* **2022**, *22*, 7929. [CrossRef]
53. Aragbaiye, Y.M.; Isleifson, D. Mass Reduction Techniques for Short Backfire Antennas: Additive Manufacturing and Structural Perforations. *Sensors* **2023**, *23*, 8765. [CrossRef]
54. Hong, S.; Kim, Y.; Won Jung, C. Transparent Microstrip Patch Antennas With Multilayer and Metal-Mesh Films. *IEEE Antennas Wirel. Propag. Lett.* **2017**, *16*, 772–775. [CrossRef]
55. Silva, Z.J.; Hunter, C.P.; Valenta, C.R.; Durgin, G.D. 2.5 GHz Meshed Inset-Fed Patch Antenna. In Proceedings of the 2019 IEEE International Symposium on Antennas and Propagation and USNC-URSI Radio Science Meeting, Atlanta, GA, USA, 7–12 July 2019; pp. 843–844. [CrossRef]